11-21-2016

Synthesis, X-ray Structures, Electronic Properties, and O_2/NO Reactivities of Thiol Dioxygenase Active-Site Models

Anne A. Fischer
Marquette University

Nuru Stracey
University of Wisconsin - Madison

Sergey V. Lindeman
Marquette University, sergey.lindeman@marquette.edu

Thomas C. Brunold
University of Wisconsin - Madison

Adam T. Fiedler
Marquette University, adam.fiedler@marquette.edu

Synthesis, X-ray Structures, Electronic Properties, and O₂/NO Reactivities of Thiol Dioxygenase Active-Site Models

Anne A. Fischer
Department of Chemistry, Marquette University, Milwaukee, WI

Nuru Stracey
Department of Chemistry, University of Wisconsin—Madison, Madison, WI

Sergey V. Lindeman
Department of Chemistry, Marquette University, Milwaukee, WI

Thomas C. Brunold
Department of Chemistry, University of Wisconsin—Madison, Madison, WI

Adam T. Fiedler
Department of Chemistry, Marquette University, Milwaukee, WI

Synopsis: Synthetic models of the thiol dioxygenases (TDOs) have been prepared using a tris(imidazolyl)phosphine ligand that reproduces the atypical three histidine triad of the enzyme active sites. Geometric- and electronic-structure descriptions were obtained with crystallographic, spectroscopic, and computational methods. Dioxygen reactivity experiments confirmed that the complexes behave as functional TDO models, and insights into the O_2 activation mechanism were derived from kinetic studies and DFT. Exposure to NO yields multiple mono- and dinitrosyl iron complexes.

Abstract
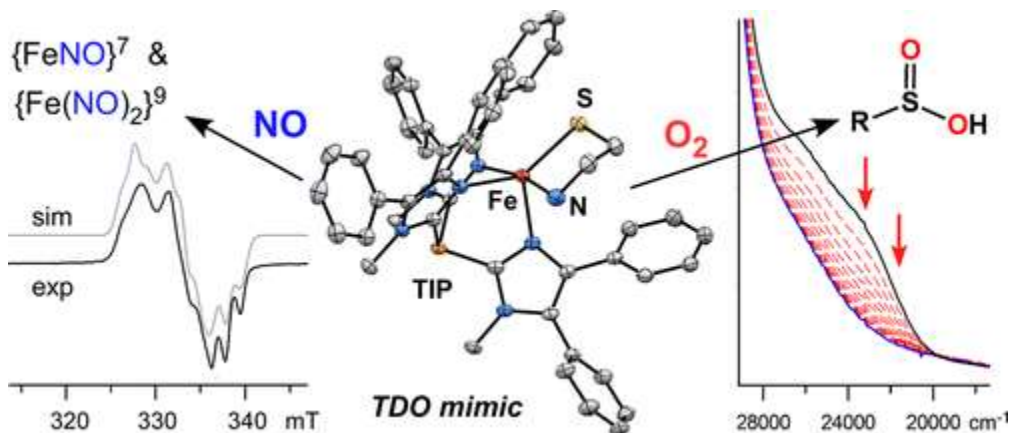
Mononuclear non-heme iron complexes that serve as structural and functional mimics of the thiol dioxygenases (TDOs), cysteine dioxygenase (CDO) and cysteamine dioxygenase (ADO), have been prepared and characterized with crystallographic, spectroscopic, kinetic, and computational methods. The high-spin Fe(II) complexes feature the facially coordinating tris(4,5-diphenyl-1-methylimidazol-2-yl)phosphine (^{Ph2}TIP) ligand that replicates the three histidine (3His) triad of the TDO active sites. Further coordination with bidentate l-cysteine ethyl ester (CysOEt) or cysteamine (CysAm) anions yielded five-coordinate (5C) complexes that resemble the substrate-bound forms of CDO and ADO, respectively. Detailed electronic-structure descriptions of the [Fe(^{Ph2}TIP)($L_{S,N}$)]BPh$_4$ complexes, where $L_{S,N}$ = CysOEt (**1**) or CysAm (**2**), were generated through a combination of spectroscopic techniques [electronic absorption, magnetic circular dichroism (MCD)] and density functional theory (DFT). Complexes **1** and **2** decompose in the presence of O_2 to yield the corresponding sulfinic acid (RSO$_2$H) products, thereby emulating the reactivity of the TDO enzymes and related complexes. Rate constants and activation parameters for the dioxygenation reactions were measured and interpreted with the aid of DFT calculations for O_2-bound intermediates. Treatment of the TDO models with nitric oxide (NO)—a well-established surrogate of O_2—led to a mixture of high-spin and low-spin {FeNO}[7] species at low temperature (−70 °C), as indicated by electron paramagnetic resonance (EPR) spectroscopy. At room temperature, these Fe/NO adducts convert to a common species with EPR and infrared (IR) features typical of cationic dinitrosyl iron complexes (DNICs). To complement

these results, parallel spectroscopic, computational, and O_2/NO reactivity studies were carried out using previously reported TDO models that feature an anionic hydrotris(3-phenyl-5-methyl-pyrazolyl)borate ($^{Ph,Me}Tp^-$) ligand. Though the O_2 reactivities of the ^{Ph2}TIP- and $^{Ph,Me}Tp$-based complexes are quite similar, the supporting ligand perturbs the energies of Fe 3d-based molecular orbitals and modulates Fe–S bond covalency, suggesting possible rationales for the presence of neutral 3His coordination in CDO and ADO.

1 Introduction

The catabolism of a diverse array of cellular compounds depends upon mononuclear non-heme iron dioxygenases (MNIDs) that incorporate both atoms of O_2 into the product(s).[1,2] The best-known MNIDs are bacterial enzymes that catalyze the oxidative cleavage of aromatic and aliphatic C–C bonds and play a central role in the degradation of environmental pollutants (i.e., biodegradation).[3-5] MNIDs are also involved in human metabolism, as exemplified by cysteine dioxygenase (CDO) and cysteamine dioxygenase (ADO).[6-8] Both enzymes are thiol dioxygenases (TDOs) that convert an alkylthiol (RSH) to the corresponding sulfinic acid (RSO_2H) using O_2 (Scheme 1). CDO regulates the cellular concentration of l-cysteine (Cys) by performing the first step in the catabolism of this amino acid that leads to the formation of either taurine or sulfate as the end product.[9,10] Insufficient levels of CDO activity cause exogenous Cys to accumulate to deleterious levels, and this metabolic imbalance is associated with several neurological disorders, including Parkinson's and Alzheimer's diseases,[11-14] as well as autoimmune disorders.[15,16] ADO is required for the degradation of coenzyme A in mammals, and is the major contributor to the production of (hypo)taurine in the brain where levels of CDO are low.[6,17]
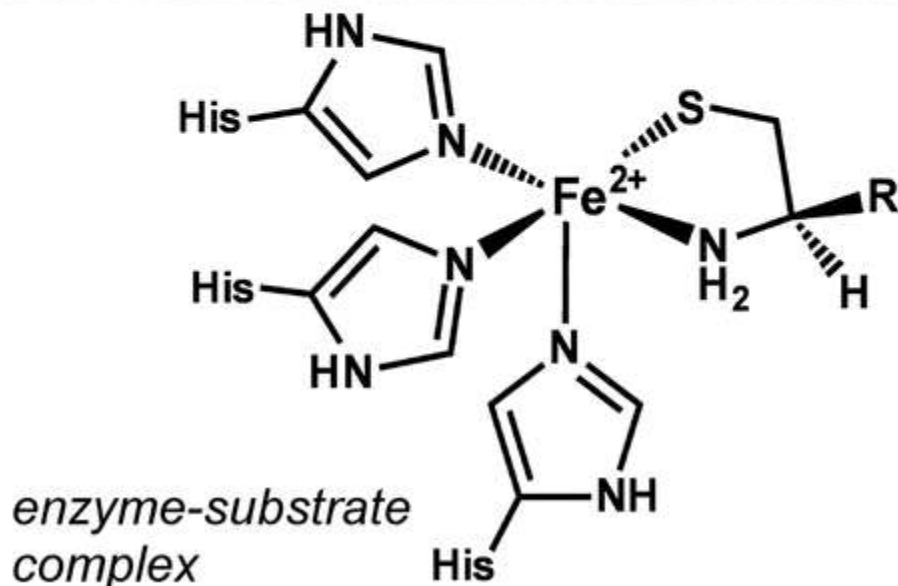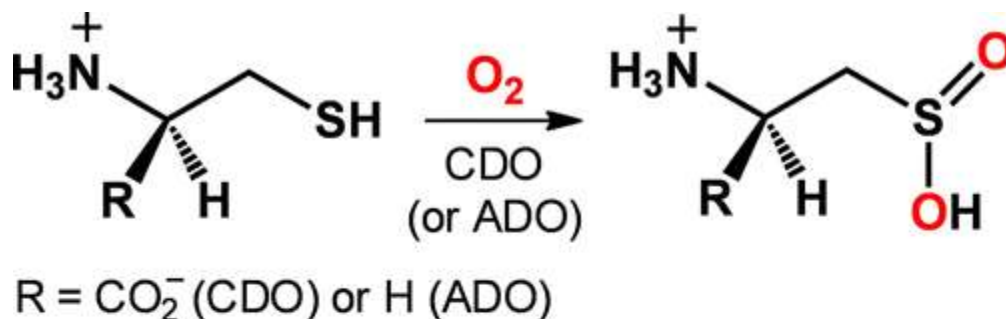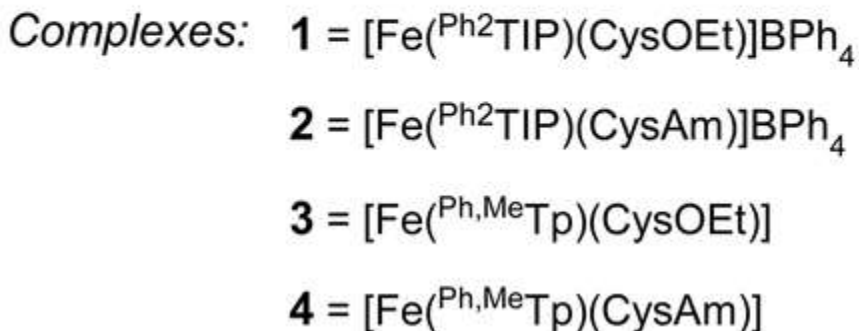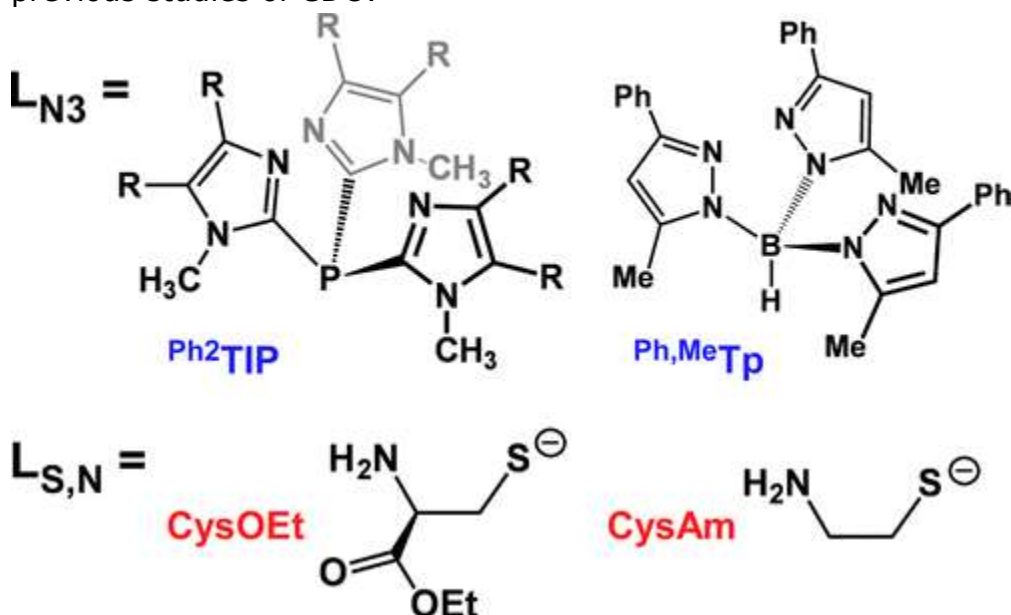
Scheme 1

Beyond its medical importance, CDO has attracted attention due to its atypical active-site structure. The overwhelming majority of MNIDs feature a high-spin Fe(II) center bound by one Asp (or Glu) and two His residues in a facial orientation (i.e., the 2-His-1-carboxylate (2H1C) facial triad).[18,19] In contrast, crystal structures of CDO have revealed a mononuclear Fe site with a neutral 3-histidine (3His) facial triad (Scheme 1).[20,21] The X-ray crystallographic data confirmed that Cys binds directly to Fe in a bidentate manner via its thiolate and amine donors, yielding a five-coordinate (5C) Fe(II) site capable of O_2 binding.[22] While a crystal structure of ADO is currently lacking, sequence analysis suggests that it features a similar active-site structure.[17] Since the publication of the first CDO structure in 2006, the 3His triad has also been observed in three microbial MNIDs: β-diketone dioxygenase (Dke1),[23-25] gentisate dioxygenase (GDO),[26] and salicylate dioxygenase (SDO).[27] The catalytic implications of this

alteration in the first-sphere coordination sphere (3His vs 2H1C triad) have been widely discussed, but no consensus explanation has emerged.[28]

The first biomimetic models of CDO, prepared by Goldberg and co-workers, were based on 2,6-bis(imino)pyridine frameworks that provide three neutral *N*-donors in a meridional arrangement.[29-32] These complexes feature an exogenous or pendant aryl thiolate ligand that converts to a sulfonato (RSO_3^-) donor upon exposure to O_2. The same group has utilized the pentadentate N4S chelate, N3PyS, to prepare TDO models in which the aryl thiolate is appended to a tripodal scaffold.[33] Reaction of the resulting Fe(II) complex, [Fe(N3PyS)(MeCN)]$^+$, with O_2 leads to double oxygenation of the thiolate donor, thereby mimicking the thiolate-to-sulfinate conversion catalyzed by CDO. Treatment of the same complex with nitric oxide (NO) generates a stable $\{FeNO\}^7$ species that exhibits spectroscopic properties similar to those observed for the low-spin ($S = 1/2$) NO adduct of substrate-bound CDO.[34,35] Recently, Limberg and co-workers have prepared structural and functional CDO and ADO mimics supported by the hydrotris(3-phenyl-5-methylpyrazolyl)borate (^{Ph,Me}Tp$^-$) ligand and featuring bidentate l-cysteine ethyl ester (CysOEt) or cysteamine (CysAm) anions, respectively.[36-38] These 5C Fe(II) complexes react with O_2 to give the *S*-dioxygenated products, as confirmed by experiments involving isotopically labeled O_2. De Visser and others have explored the O_2-activation mechanisms of CDO and select TDO models using computational methods.[39-42]

While these previous biomimetic studies of CDO and ADO have yielded many exciting results, the models reported to date lack either the facial geometry or neutral charge of the 3His triad. As part of our efforts to prepare faithful Dke1 and GDO models, our group has found that easily prepared tris(imidazolyl)phosphine (TIP) ligands nicely replicate the *fac* arrangement of three imidazole donors found in the active sites.[43-46] Here, we report the synthesis and structural characterization of two TDO models: [Fe(^{Ph2}TIP)(CysOEt)]BPh$_4$ (**1**) and [Fe(^{Ph2}TIP)(CysAm)]BPh$_4$ (**2**), where ^{Ph2}TIP is tris(4,5-diphenyl-1-methylimidazol-2-yl)phosphine (Scheme 2). These complexes are related to the TDO mimics of Limberg and co-workers (**3** and **4** in Scheme 2); the critical difference is that **1** and **2** feature a neutral TIP

scaffold, whereas **3** and **4** employ a monoanionic ^Ph,Me^Tp⁻ ligand. Our previous studies of Dke1 models indicated that TIP ligands accurately reproduce the coordination environment and donor strength of the 3His triad, whereas the properties of Tp⁻ ligands align better with the 2H1C triad.[43] Since the two sets of models are complementary, we have conducted parallel studies of **1/2** and **3/4** with the goal of illuminating the role of 3His coordination in promoting CDO/ADO catalysis. Therefore, this manuscript describes and compares the geometric structures, electronic properties, and O_2 reactivities of complexes **1**–**4**, as revealed through a combination of crystallographic, spectroscopic, kinetic, and computational methods. The similitude of these models to the enzyme active site is evaluated by juxtaposing their structural and spectroscopic features to those reported in previous studies of CDO.

Scheme 2

Formation of an iron–superoxo intermediate is the putative first step of O_2 activation in both TDOs and related complexes; however, the spin state and degree of S-radical character in the Fe/O_2 adduct remain matters of debate. In this report, the nature of O_2-bound **2** and **4** in various spin states has been probed via density functional theory (DFT) calculations, with a particular focus on the effect of ligand charge (TIP vs Tp^-) on energetics and Fe–S covalency. We have also explored the surprisingly complicated reactivity of **1** and **2** with NO, a well-established surrogate for O_2. Electron paramagnetic resonance (EPR) and IR experiments revealed that multiple Fe/NO species (both high- and low-spin) are formed, including a cationic dinitrosyl iron complex (DNIC). These results highlight the hemilability of scorpionate chelates, as well as the critical role of the active-site pocket in controlling the relative positioning of first-sphere ligands in CDO and ADO.

2 Experimental and Computational Methods

2.1 General Information

Unless otherwise noted, all reagents and solvents were purchased from commercial sources and used as received. Dichloromethane (CH_2Cl_2) was purified and dried using a Vacuum Atmospheres solvent purification system and stored under N_2. The synthesis and handling of air-sensitive materials were performed under inert atmosphere using a Vacuum Atmospheres Omni-Lab glovebox equipped with a freezer set to -30 °C. Nitric oxide (NO) from a cylinder (Airgas, Inc.) was purified by passage through an ascarite II column, followed by a cold trap at -78 °C to remove higher N_xO_y impurities. ^{15}N-labeled NO was prepared via reaction of $Na^{15}NO_2$ with ascorbic acid and aqueous Cu(II) chloride under an argon (Ar) atmosphere.[47] The L_{N3} supporting ligands $K(^{Ph,Me}Tp)$ and ^{Ph2}TIP, as well as complexes **3** and **4**, were prepared according to literature procedures.[36,37,44,48]

2.2 Physical Methods

Elemental analyses were performed at Midwest Microlab, LLC, in Indianapolis, IN. UV–vis absorption spectra were collected with an

Agilent 8453 diode array spectrometer equipped with a cryostat from Unisoku Scientific Instruments (Osaka, Japan) for experiments at reduced temperatures. Infrared (IR) spectra were measured with a Nicolet Magna-IR 560 spectrometer. X-band EPR experiments were performed using a Bruker EleXsys E650 instrument equipped with an ER4415DM cavity, an Oxford Instruments ITC503 temperature controller, and an ESR-900 He flow cryostat. The program *EasySpin* (version 5) was used to simulate the experimental spectra.[49] ^{1}H NMR spectra were recorded in deuterated solvents using a Varian 400 MHz spectrometer. Mass spectrometric data were measured using either an Agilent 6850 gas chromatography–mass spectrometer (GC–MS) with a HP-5 column or a Bruker matrix-assisted laser desorption/ionization (MALDI) time-of-flight (TOF) microflex instrument. Magnetic circular dichroism (MCD) data were collected using a Jasco model J-715 spectropolarimeter, in conjunction with an Oxford Instrument SM-4000 8T magnetocryostat. The samples for these studies were prepared in CH_2Cl_2 and then diluted with butyronitrile to a final ratio of 3:7 (v/v), or 1:1 (v/v) for the NO-treated samples, thereby yielding glassy solutions upon freezing in liquid nitrogen. Potential artifacts due to glass strain were eliminated by taking the difference between spectra collected with the magnetic field aligned parallel and antiparallel to the direction of light propagation.

X-ray diffraction (XRD) data were collected at 100 K with an Oxford Diffraction SuperNova kappa-diffractometer (Rigaku Corp.) equipped with dual microfocus Cu/Mo X-ray sources, X-ray mirror optics, an Atlas CCD detector, and a low-temperature Cryojet device. The data were processed with the CrysAlis Pro program package, followed by numerical absorption correction based on Gaussian integration over a multifaceted crystal model and then empirical absorption correction using spherical harmonics, as implemented in SCALE3 ABSPACK scaling algorithm. Structures were solved using the SHELXS program and refined with the SHELXL program[50] within the Olex2 crystallographic package.[51] X-ray crystallographic parameters are provided in Table S1, and further experimental details are available in the CIFs.

2.3 [Fe(^{Ph2}TIP)(CysOEt)]BPh$_4$ (**1**)

l-Cysteine ethyl ester hydrochloride (38 mg, 0.20 mmol) and triethylamine (62 µL, 0.44 mmol) were combined in CH_2Cl_2 and stirred until the solid completely dissolved. A solution of the [Fe(^{Ph2}TIP)(MeCN)$_3$](OTf)$_2$ precursor[44] (0.242 g, 0.20 mmol) in CH_2Cl_2 was added dropwise, giving rise to a bright yellow solution, which was stirred for 30 min. The solvent was removed under vacuum, and the resulting yellow residue was taken up in MeOH and filtered. Addition of NaBPh$_4$ (68 mg, 0.20 mmol) caused immediate formation of a yellow precipitate. After solvent removal under vacuum, the resulting yellow powder was dissolved in a minimal amount of 1,2-dichloroethane and layered with MeOH. The yellow needles that formed after 1 day were collected, washed with MeOH, and dried under vacuum. Yield = 0.138 g (55%). X-ray quality crystals were obtained by allowing the mother liquor to stand for 1 week at room temperature and under inert atmosphere. Crystallographic analysis revealed the presence of a MeOH solvate in the unit cell. Elemental analysis calculated (%) for $C_{77}H_{69}BFeN_7O_2PS·CH_3OH$: C, 72.84; H, 5.72; N, 7.62. Found: C, 72.56; H, 5.61; N, 7.70. IR (solution in CH_2Cl_2, cm^{-1}): ν = 3345 (w, ν(N–H)), 1728 (s, ν(C=O)). ^{1}H NMR (400 MHz, CDCl$_3$): δ = 15.54 (s, 1H, −N*H*), 15.14 (s, 1H, −N*H*), 14.86 (s, 9H, *N*–C*H$_3$*), 8.08 (s, 3H), 7.63 (s, 12H, BPh$_4$), 6.90 (s, 6H), 6.37 (s, 8H, BPh$_4$), 6.04 (s, 6H), 4.22 (s, 6H), 2.96 (q, 2H, −CO$_2$C*H$_2$*CH$_3$), 2.41 (broad s, 2H, −SC*H$_2$*C−), 2.01 (s, 1H, −H$_2$NC*H*−), 1.31 (t, 3H, −COOCH$_2$C*H$_3$*), −17.46 (broad s, 6H) ppm.

2.4 [Fe(^{Ph2}TIP)(CysAm)]BPh$_4$ (**2**)

Cysteamine hydrochloride (23 mg, 0.20 mmol) and triethylamine (62 µL, 0.44 mmol) were combined in CH_2Cl_2 and stirred until all the solid dissolved. A solution of [Fe(^{Ph2}TIP)(MeCN)$_3$](OTf)$_2$ (0.242 g, 0.20 mmol) in CH_2Cl_2 was added dropwise, giving an orange solution, which was stirred for 30 min. The solvent was removed under vacuum and the resulting yellow residue taken up in MeOH. Addition of NaBPh$_4$ (68 mg, 0.20 mmol) caused immediate formation of a yellow precipitate. After evaporation of the solvent under vacuum, the resulting yellow powder was dissolved in a minimal amount of 1,2-dichloroethane and layered with MeOH. X-ray quality yellow crystals formed after 1 day at room temperature. The crystals were collected,

washed with MeOH, and dried under vacuum. Yield = 0.015 g (18%). Elemental analysis calculated (%) for $C_{74}H_{65}BFeN_7PS$: C, 75.19; H, 5.54; N, 8.29. Found: C, 76.02; H, 6.02; N, 7.89. IR (solution in CH_2Cl_2, cm^{-1}): ν = 3353 (w, ν(N–H)). ^1H NMR (400 MHz, $CDCl_3$): δ = 14.86 (s, 9H, *N*-1-C*H₃*), 8.19 (s, 8H, BPh_4), 8.05 (s, 4H, BPh_4), 7.34 (s, 8H, BPh_4), 6.85 (s, 6H), 6.03 (s, 3H), 5.93 (s, 3H), 4.08 (s, 6H), 3.89 (s, 2H, −N*H₂*), 3.21 (s, 6H), 2.63 (t, 1H, −CH₂CH₂−), 1.35 (t, 1H, −CH₂CH₂−), 1.23 (t, 1H, −CH₂CH₂−), 1.13 (t, 1H, −CH₂CH₂−), −19.26 (broad s, 6H, *o*-4-Ph) ppm.

2.5 Reactivity with Dioxygen

Rate measurements were generally performed under conditions of O_2 saturation by bubbling O_2 (Airgas, Inc.) through CH_2Cl_2 solutions of **1** or **3** for several minutes.

For both complexes, rates of reaction were measured four times at 20 °C, and changes in absorption intensity at two wavelengths were fit to exponential curves using the program IGOR. The reported k_1 values and uncertainties correspond to the averages and standard deviations, respectively, of the resulting pseudo-first-order rate constants. The concentration of O_2 in solution at various temperatures (*T*) was estimated using the formula $S = (LP_{O2})/(TR)$, where *L* is the Ostwald coefficient (0.257 for CH_2Cl_2), P_{O2} is the partial pressure of O_2, and *R* is the gas constant.[52,53] The determination of P_{O2} accounted for the vapor pressure of CH_2Cl_2 (P_{solv}) as a function of *T*: P_{O2} = 1 atm − P_{solv}. Lower concentrations of O_2 were obtained by injecting anaerobic solutions of the Fe(II) complex into O_2-saturated solutions of CH_2Cl_2 in varying amounts. Following established procedures,[36,37] the products of the oxygenation reactions were isolated by addition of 3M HCl to the reaction mixture and stirred for 3 h. The aqueous layer was collected and the solvent removed under vacuum. The remaining residue was dissolved in MeOH and stirred with Chelex for 12 h. The solvent was removed by vacuum after filtration, and the resulting white solid was washed with toluene. ^1H NMR data of the reaction products were interpreted with the aid of published spectra and/or by comparison to spectra measured with commercially available material. Product of **1** + O_2 reaction: yield = 48%. ^1H NMR (400 MHz, CD_3OD): δ = 1.28 (t, 3H, −OCH₂C*H₃*), 2.49 (dd, 1H, −C*H₂*S), 2.61 (dd, 1H, −C*H₂*S), 4.02 (m, 1

H, −CHNH$_2$), 4.20 (q, 2H, −OCH_2CH$_3$) ppm. MALDI-TOF data (*m/z*): {M}$^+$ calcd for C$_5$H$_{11}$NO$_4$S 181.21, found 180.94; {M − CH$_3$}$^+$ calcd for C$_4$H$_8$NO$_4$S 166.18, found 165.76. Product of **2** + O$_2$ reaction: yield = 61%. ^{1}H NMR (400 MHz, CD$_3$OD): δ = 2.45 (t, 2H, −CH_2S), 3.15 (t, 2H, −CH_2NH$_2$) ppm.

2.6 Density Functional Theory (DFT) Computations

Electronic-structure calculations were carried out using the ORCA 3.0 software package developed by Dr. F. Neese (MPI for Chemical Energy Conversion).[54] Computational models of **2** and **4** were obtained via unstrained DFT geometry optimizations, using the X-ray crystal structures as starting points. For calculations involving **2**, the ^{Ph2}TIP ligand was truncated by replacing the 4,5-diphenyl-1-methylimidazole donors with 4-methylimidazole rings; similarly, in calculations for **4** the ^{Ph,Me}Tp$^-$ ligand was modeled as ^{Me,H}Tp$^-$. Numerical frequency calculations verified that all structures corresponded to a local minimum with only real vibrational frequencies. The zero-point energies, thermal corrections, and entropy terms (vibrational, rotational, translational) were obtained from these frequency calculations. All calculations were carried out spin-unrestricted and utilized the Ahlrichs valence triple-ζ basis set (TZV) and TZV/J auxiliary basis set, in conjunction with polarization functions on main-group and transition-metal elements (default-basis 3 in ORCA).[55-57] Solvent effects were accounted for using the conductor-like screening model (COSMO)[58] with a dielectric constant (ε) of 9.08 for CH$_2$Cl$_2$.

The DFT calculations employed different functionals depending on the nature of the species under examination and the property being computed. Geometric structures for the Fe(II) complexes and Fe/O$_2$ adducts were optimized using the Perdew–Burke–Ernzerhof (PBE) functional[59] with 10% Hartree–Fock exchange. The "spin-flip" feature of ORCA was employed to generate broken-symmetric wave functions for the S_{tot} = 2 and 1 states of Fe/O$_2$ adducts containing high-spin Fe centers. The transition state for the S–O$_d$ bond forming reaction (where O$_d$ is the distal oxygen atom of the iron–superoxo unit) was located by performing a relaxed surface scan along the S⋅⋅⋅O$_d$ distance. The existence of the transition state was confirmed by the presence of one imaginary frequency, corresponding to the ν(S–O$_d$) mode.

Calculations of the Fe/NO adducts employed either the Becke–Perdew (BP86)[60,61] or TPSSh[62,63] functionals. In calculations of EPR parameters, the "core properties" with extended polarization [CP(PPP)] basis set[64] was used for the Fe atom and Kutzelnigg's NMR/EPR (IGLO-III) basis set[65] for the NO ligand. The contribution of spin–orbit coupling to the **g**- and **A**-tensors was evaluated by solving the coupled-perturbed self-consistent field (CP-SCF) equations.[66-69] To compute the hyperfine coupling constants, a high resolution grid with an integration accuracy of 7.0 was used for the Fe and N atoms. Time-dependent DFT (TD-DFT) calculations employed the cam-B3LYP range-separated hybrid functional,[70] previously shown to yield good agreement between experimental and TD-DFT computed absorption spectra for CDO.[71] Absorption energies and intensities were computed for 40 excited states with the Tamm–Dancoff approximation.[72,73] Isosurface plots of molecular orbitals were prepared using the *ChemCraft* program.

3 Results and Discussion

3.1 Synthesis and Solid State Structures

Complexes **1** and **2** were synthesized by first treating the previously reported [Fe(^{Ph2}TIP)(MeCN)$_3$](OTf)$_2$ precursor[44] with either CysOEt·HCl or CysAm·HCl and 2 equiv of triethylamine in CH_2Cl_2. After solvent removal, the resulting triflate salts were dissolved in MeOH and addition of NaBPh$_4$ caused immediate precipitation of **1** and **2** as bright yellow solids. X-ray quality crystals of **2** were grown by layering concentrated 1,2-dichloroethane (DCE) solutions with MeOH. In the case of **1**, this procedure yielded analytically pure but poorly diffracting needles; however, crystals suitable for X-ray analysis were eventually obtained by allowing the decanted mother liquor to sit for 1 week. The resulting crystal structure revealed that, during this time, the CysOEt ligand had undergone transesterification to give the complex [Fe(^{Ph2}TIP)(CysOMe)]BPh$_4$ (**1^{Me}**) instead. Despite this, ^{1}H NMR spectra of the first crop of crystals, which were employed in all spectroscopic and reactivity studies, indicated retention of the ethyl substituent (*vide infra*).

The X-ray structures of **1^Me** and **2** reveal the presence of 5C monoiron(II) complexes with a bidentate *S,N*-cysteinato anion and κ^3-^{Ph2}TIP chelate (Figure 1). In each case, the thiolate donor forms a hydrogen bond with a MeOH solvate molecule. The Fe(II) coordination geometries lie halfway between the square-pyramidal and trigonal bipyramidal limits, as quantified by the τ-values of 0.54 (**1^Me**) and 0.55 (**2**).[74] Significantly, the facial coordination mode of the ^{Ph2}TIP ligand ensures that a vacant site for O_2-binding is available *cis* to the thiolate ligand, a known requirement for dioxygenation of the sulfur atom.[31] Selected metric parameters for the solid-state structures of **1^Me** and **2** are provided in Table 1, in addition to previously reported values for **3** and **4**. The Fe–N$_{TIP}$ bond distances are typical for high-spin Fe(II) complexes and fall within a narrow range of 2.15–2.20 Å. The Fe–N$_{Tp}$ distances in **3** and **4** are slightly shorter on average, while also displaying greater variation with two short bonds of 2.12 Å (av) and one long bond near 2.275 Å. The Fe–S1 and Fe–N$_{Cys}$ bond distances change little across the **1**–**4** series with average values of 2.31 and 2.26 Å, respectively.
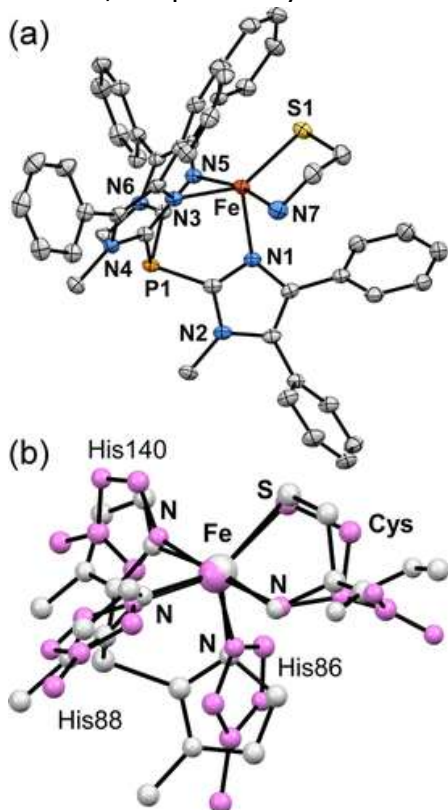
Figure 1. (a) Thermal ellipsoid plot (50% probability) obtained from the X-ray crystal structure of **2**. The BPh$_4^-$ counteranion, noncoordinating solvent molecules, and all

hydrogen atoms have been omitted for clarity. (b) Overlays of the crystallographically derived structures of **1^Me** (light gray) and the Cys-bound active site of CDO (pink) derived from PDB 4TJO. The phenyl substituents of the TIP^Ph2 ligand are not shown.

Table 1. Selected Bond Distances (Å) and Bond Angles (deg) for Complexes **1**−**4** and the Cys-Bound CDO Active Site as Determined by X-ray Crystallography

	1	**2**	**3[a]**	**4[b]**	**CDO[c]**
		Bond Distances			
Fe1−N1	2.170(2)	2.169(2)	2.112(2)	2.153(2)	1.893
Fe1−N3	2.153(2)	2.178(2)	2.106(2)	2.110(2)	2.199
Fe1−N5	2.195(2)	2.183(2)	2.275(2)	2.249(2)	2.110
Fe1−S1	2.3107(6)	2.3051(5)	2.3122(9)	2.3175(6)	2.291
Fe1−N7	2.245(2)	2.248(2)	2.290(3)	2.252(2)	2.262
		Bond Angles			
N1−Fe1−N3	96.73(6)	98.67(6)	95.36(9)	95.97(6)	99.9
N1−Fe1−N5	87.90(6)	86.32(6)	82.29(9)	86.08(6)	98.6
N1−Fe1−S1	125.08(5)	120.73(4)	134.21(7)	129.17(5)	112.9
N1−Fe1−N7	89.01(6)	88.43(6)	89.30(9)	90.71(6)	85.7
N3−Fe1−N5	83.02(6)	82.88(6)	85.29(9)	82.16(6)	86.0
N3−Fe1−S1	137.22(5)	139.15(4)	130.07(7)	134.18(5)	146.8
N3−Fe1−N7	87.80(6)	86.20(6)	92.04(9)	87.38(7)	96.9
N5−Fe1−S1	104.99(4)	108.23(4)	104.07(6)	105.47(5)	94.1
N5−Fe1−N7	169.90(6)	167.03(6)	170.88(9)	168.67(6)	174.3
S1−Fe1−N7	84.63(5)	84.64(4)	84.32(7)	84.96(5)	80.8

[a]Reference.[36]
[b]Reference.[37]
[c]Obtained from an X-ray structure of Cys-bound CDO (PDB 4JTO; 2.0 Å resolution).

The superposition of complex **1^Me** upon the active-site structure of Cys-bound Fe(II)−CDO[75] in Figure 1b highlights the structural similarities between the synthetic and enzymatic coordination environments. The most noticeable discrepancy concerns the relative orientations of the imidazole rings. The His donors in the enzyme active site possess greater rotational freedom than their synthetic counterparts, as the latter are tethered to a central P atom at the 2-position. The CDO crystal structure exhibits Fe−N$_{His}$ distances of 2.20, 2.11, and 1.89 Å (Table 1); the smallest value (corresponding to His86) is much shorter than expected based on synthetic CDO models and typical Fe−N$_{His}$ bond distances in proteins.[76] The Fe−N$_{Cys}$ and Fe−S$_{Cys}$ bond distances of CDO nicely match those measured for **1^Me** (Table 1), and the orientations of the cysteinato ligands with respect to the facial N3 triad are quite similar, although CDO lies somewhat

closer to the square-pyramidal limit (τ-value of 0.46). The high degree of structural resemblance between CDO and **1^Me** suggests that these five-coordinate sites are similarly primed for O_2 activation.

3.2 Solution-State Spectroscopic Properties

Examination of $CDCl_3$ solutions of **1** and **2** using the Evans NMR method provided effective magnetic moments of 5.16 and 5.02 μ_B, respectively, consistent with mononuclear, high-spin ($S = 2$) ferrous complexes. The ^1H NMR spectra of **1** and **2** exhibit paramagnetically shifted peaks in the 15 to −20 ppm range (Figures S1 and S2). The three imidazole donors are spectroscopically equivalent due to dynamic averaging of the CysOEt/CysAm positions on the NMR time scale. Based on our prior analysis of ^{Ph2}TIP-based Fe(II) complexes,[44] the intense downfield peak at 15 ppm is assigned to the N-1-CH_3 groups, while the broad upfield peak near −18 ppm is attributed to *ortho* protons of the 4-Ph substituents. Resonances arising from the CysOEt and CysAm ligands experience only modest shifts and broadening upon ligand binding to Fe. The splitting pattern due to the ethyl ester moiety is clearly discernible in the spectrum of **1**, indicating that the CysOEt ligand remains intact. In short, the ^1H NMR data confirm that the solution- and solid-states structures are essentially the same.

Solutions of **1** and **2** in CH_2Cl_2 are pale yellow due to the presence of overlapping absorption bands ($\varepsilon \sim 1000$ M^{-1} cm^{-1}) in the near-UV region that are attributed to S → Fe(II) charge transfer (CT) transitions (*vide infra*). To obtain further information regarding the electronic excited states of these complexes, magnetic circular dichroism (MCD) spectra of **1** and **2** were measured in frozen 3:7 solutions of CH_2Cl_2:butyronitrile. The absorption and MCD spectra of the two complexes are nearly identical, suggesting that the cysteinato substituent (−CO_2Et or −H) has little effect on overall electronic structure. As shown in Figures 2 and S3, the MCD spectra exhibit two intense, positive features near 23,800 and 26,800 cm^{-1}. The broadness of the lower-energy band suggests that it is composed of at least two electronic transitions. In all cases, the intensities of the MCD bands increase with decreasing temperature, displaying the *C*-term behavior expected for paramagnetic $S = 2$ systems. Significantly, the

MCD spectra of **1** and **2** also exhibit a temperature-dependent band at 11,270 cm^{-1} (887 nm) that is barely perceptible in the absorption spectra. Based on its large C_0/D_0 ratio of ~2.0 (where C_0 and D_0 are related to the MCD and absorption intensities, respectively[77]), this peak likely arises from an Fe(II) d–d transition. This assignment is supported by previous spectroscopic studies, which revealed that the highest-energy d–d transition of 5C Fe(II) complexes lies between 8,400 and 13,500 cm^{-1}.[78]
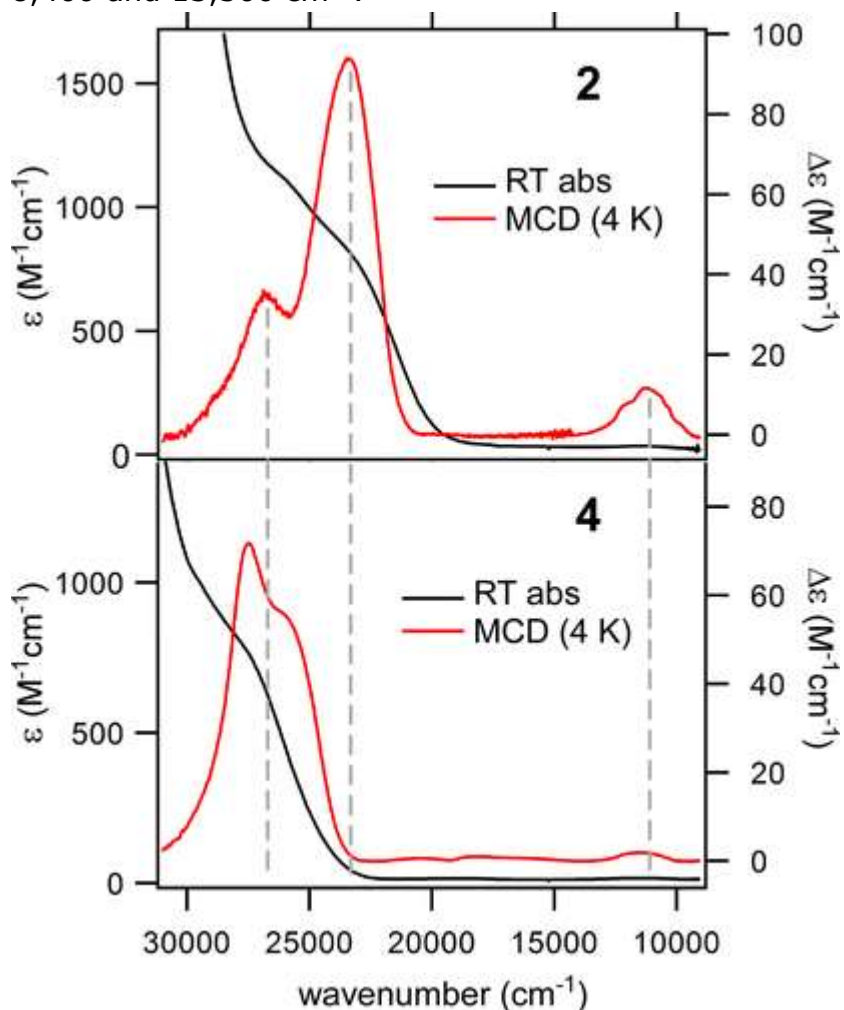
Figure 2. Electronic absorption and MCD spectra collected for complexes **2** (top) and **4** (bottom). The absorption spectra were measured at room temperature in CH$_2$Cl$_2$. The MCD spectra were obtained for frozen, glassy solutions in a 3:7 mixture (v/v) of CH$_2$Cl$_2$:butyronitrile at 4 K with a magnetic field of 7 T.

For the sake of comparison, Figure 2 also displays the absorption and MCD spectra of complex **4** measured under identical conditions. Only two S → Fe(II) CT bands are apparent, and these are

blue-shifted by 2700 cm^{-1} relative to those of complex **2**. The d–d band experiences a smaller energy increase of 300 cm^{-1}. Similar shifts in band energies are observed when spectra of CysOEt-containing **1** and **3** are compared (Figure S3).

3.3 Computational Analysis of Fe(II) Complexes

The spectroscopic results were interpreted with the aid of time-dependent DFT (TD-DFT) studies that employed the cam-B3LYP range-separated hybrid functional.[70] These calculations were performed with geometry-optimized structures of **2** and **4** that are in good agreement with the crystallographic structures (Table S2). Consistent with the experimental data, the TD-DFT computed absorption spectrum for **2** is dominated by three S → Fe(II) CT transitions in the region below 30,000 cm^{-1} (Figure S4). The energy-level diagram provided in Figure 3 depicts the ligand- and Fe(II)-based molecular orbitals (MOs) involved in the relevant transitions. The donor MOs are localized on the CysAm ligand and contain primarily S(3p) character: the S$_\sigma$ MO lies along the Fe–S bond, while the S$_\pi$ MO is perpendicular to the bond. The two lowest-energy CT bands in the TD-DFT spectrum arise from S$_\pi$ → Fe(d$_{xz}$)/Fe(d$_{yz}$) transitions centered around 25,000 cm^{-1}, which nicely matches the experimental band at 23,800 cm^{-1}. To higher energy, TD-DFT predicts a S$_\sigma$ → Fe(II) (σ → σ*) transition at 29,100 cm^{-1} that likely corresponds to the experimental feature at 26800 cm^{-1}. The highest-energy Fe d–d transition, attributed to the Fe(d$_{xy}$) → Fe(d$_{x^2-y^2}$) excitation, is predicted to appear as a weak feature at 13,750 cm^{-1}. Thus, the calculated energies agree resonably well with the experimental values, with a root-mean-square deviation of only 2100 cm^{-1} for the bands observed by MCD.
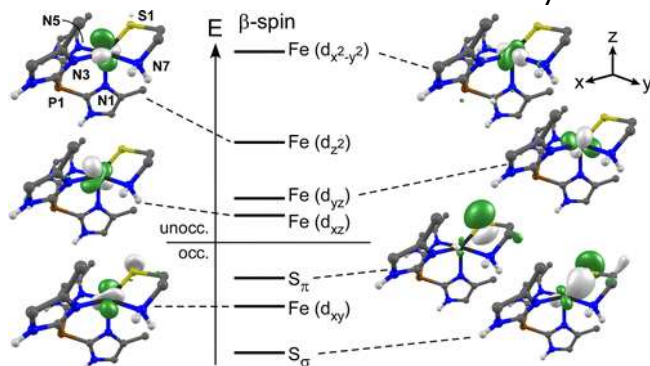
Figure 3. Energy-level diagram for the spin-down (β) molecular orbitals (MOs) obtained from a spin-unrestricted DFT calculation for complex **2**. MOs are labeled

according to their principal contributor. DFT-generated isosurface plots of the MOs are also provided.

Comparison of the DFT results obtained for **2** and **4** indicate that substitution of neutral ^{Ph2}TIP with anionic ^{Ph,Me}Tp$^-$ causes a nearly uniform 4450 cm^{-1} increase in the energies of the Fe 3d set of orbitals. Hence, the S → Fe(II) CT bands experience a substantial blue-shift upon conversion of **2** → **4**, while the highest-energy d−d transition is largely unaffected, consistent with the spectroscopic data described above. The S$_\sigma$ → Fe(II) (σ → σ*) transition of complex **4**, predicted to occur at 33,270 cm^{-1}, is likely obscured by the onset of π−π* transitions in the near-UV region, which explains the presence of only two CT bands in the absorption/MCD spectra of **3** and **4**. Moreover, an analysis of the relative compositions of the half-occupied Fe 3d-based MOs indicates that the Fe−S bond in **2** is more covalent than its counterpart in complex **4**, which is also reflected in the minor differences in the Mulliken spin populations predicted for the S atom (0.19 spin in **2** and 0.15 spin in **4**). This finding is consistent with the fact that the TIP-based complexes exhibit more intense S → Fe(II) CT transitions than the Tp-based complexes (Figures 2 and S3), given that CT intensity is proportional to the amount of ligand character in the metal-based MOs.

Substrate-bound Fe(II)−CDO likewise exhibits two S → Fe(II) CT bands in its MCD spectrum; however, both of these features appear above 30,000 cm^{-1}, much higher in energy than the corresponding bands of complexes **1**−**4**.[79] This large discrepancy in CT energies is rather surprising given the high degree of structural similarity between the first coordination spheres of **1** and Cys-bound Fe(II)−CDO, as discussed above (Figure 1). Noncovalent (e.g., electrostatic) interactions within the active site of CDO presumably modulate the relative energies of the thiolate- and Fe 3d-based MOs, thereby increasing the CT energies.

3.4 O_2 Reactivity: Experimental Results

Not surprisingly, the O$_2$ reactivity of the ^{Ph2}TIP-based complexes closely mirrors that reported previously by Limberg and co-workers for **3** and **4**. As shown in Figure 4, treatment of **1** with O$_2$ results in the slow decay of the S → Fe(II) CT bands to eventually yield a featureless

spectrum, indicating loss of the iron–thiolate bond. Similar spectral changes were observed upon O_2 exposure of complexes **3** and **4**,[36,37] as well as Cys-bound Fe(II)–CDO.[79] The reaction products were isolated after stirring solutions of **1** and **2** in O_2-saturated CH_2Cl_2 for 6 h, followed by acidic workup. ^1H NMR spectra revealed that the **1** + O_2 reaction yields the ethyl ester of l-cysteine sulfinic acid as the only observable CysOEt-derived product (Figure S5). Similarly, exposure of **2** to O_2 yields hypotaurine (HTau) as the dominant product, although an unidentified CysAm-derived compound is also present in smaller amounts (HTau:unknown ratio of 4:1; Figure S6). The identities of the sulfinic acid products were confirmed by comparison to literature spectra (cysteine sulfinic acid ethyl ester) or commercial samples (HTau), in addition to mass spectrometric analysis. Thus, each complex in the **1**−**4** series behaves as a structural *and* functional TDO mimic.
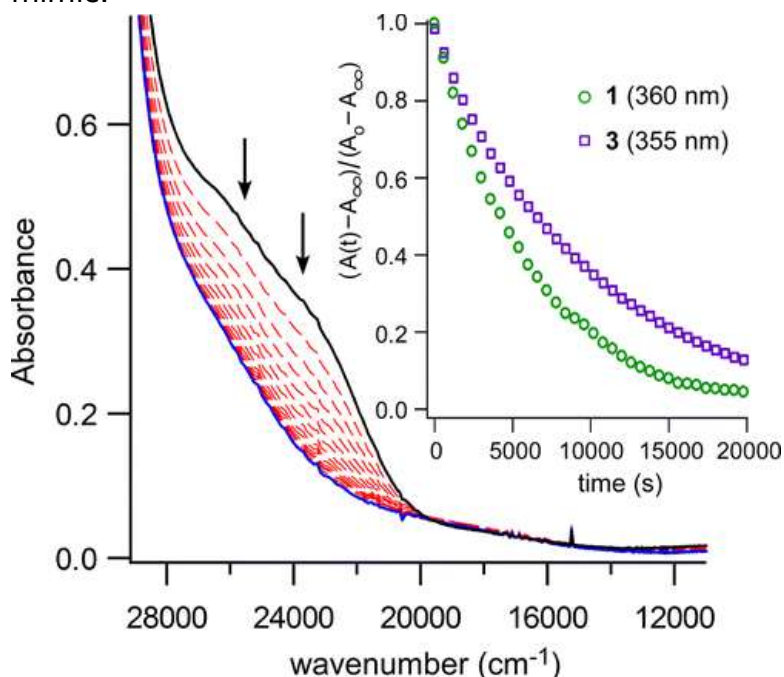

Figure 4. Time-resolved absorption spectra for the reaction of complex 1 (concentration = 0.53 mM) with O_2; the spectra shown here were collected at intervals of 30 min. The reaction was performed at 20 °C in O_2-saturated CH_2Cl_2. The path length of the cuvette was 1.0 cm. Inset: Plots of absorption intensity as a function of time for reaction of **1** and **3** with O_2 at 20 °C in O_2-saturated CH_2Cl_2. The wavelengths monitored were 360 and 355 nm for **1** and **3**, respectively. Absorption intensities were normalized using the equation provided in the plot.

Rate measurements for the reaction of **1** and **3** with O_2 were generally performed in O_2-saturated CH_2Cl_2 solutions ([O_2] = 5.8 mM

19

at 20 °C) with Fe(II) concentrations of less than 0.60 mM. Under these conditions, the decay in absorption intensity versus time followed first-order behavior past three half-lives (Figures 4 and S7) for both complexes, and initial rates increased linearly with O_2 concentration (Figure S8). Thus, the reactions are first-order with respect to both Fe and O_2, permitting a detailed kinetic analysis. At 20 °C, the **1** + O_2 reaction proceeds with a pseudo-first-order rate constant (k_1) of 1.9(4) × 10^{-4} s^{-1}. The **3** + O_2 reaction exhibits a smaller k_1-value of 1.2(3) × 10^{-4} s^{-1}.[80] Thus, the identity of the L_{N3} supporting ligand has only a modest impact on the O_2 reaction rate, with the neutral ^{Ph2}TIP ligand offering a slight rate advantage over the anionic ^{Ph,Me}Tp$^-$ ligand.

Activation parameters for the **1** + O_2 reaction were determined by monitoring rates at temperatures between 35 and −30 °C. Analysis of the linear Eyring plot (Figure 5) provided an activation enthalpy ($\Delta H^{\ddagger}$) of 12(1) kcal/mol and activation entropy ($\Delta S^{\ddagger}$) of −25(4) cal/(mol·K), resulting in an activation free energy ($\Delta G^{\ddagger}$) of 19(2) kcal/mol at 293 K. These values are similar to previously reported parameters for O_2 activation by mononuclear Fe complexes,[52] including closely related 5C complexes with ^{Ph2}TIP and Tp$^-$ ligands.[81,82] The large negative value for $\Delta S^{\ddagger}$ indicates that the rate-determining step has an associative nature, which is common for reactions involving O_2. However, as discussed in the next section, the activation parameters likely reflect multiple elementary reactions, and thus the values must be interpreted with caution.

y = -5900 x + 11.4
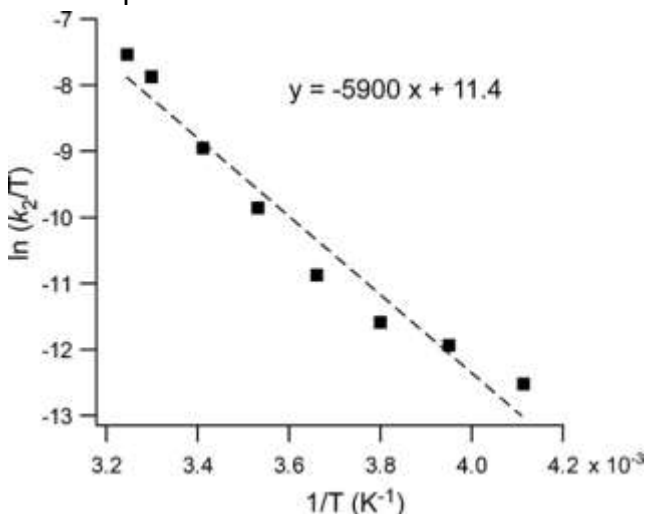
Figure 5. Eyring plot for the reaction of **1** with O_2 in O_2-saturated CH_2Cl_2 over a temperature range of 35 to −30 °C. Second-order rate constants (k_2) were obtained by dividing the pseudo-first-order rate constant by [O_2] at the specified temperature.

3.5 O_2 Reactivity: Computational Results

The first step in the proposed O_2 activation mechanisms of CDO and related model complexes is the generation of an iron–superoxo species, followed by nucleophilic attack of the distal O atom on the thiolate ligand to give a four-membered Fe–O–O–S ring. Computational studies suggested that this second step is rate-limiting in both the enzyme and complex **3**.[39,83] To better understand the kinetic data reported above, we have examined the thermodynamics of O_2 binding and O–S bond formation via DFT calculations for complexes **2** and **4**.[84] These calculations employed the PBE functional with 10% HF exchange, which has been shown to provide reliable geometries and relative energies for Fe/O_2 species.[85]

The adduct that forms upon O_2 binding to a high-spin Fe(II) complex has three possible spin states: triplet ($S = 1$), quintet ($S = 2$), or septet ($S = 3$). The septet and quintet states are best described as high-spin Fe(III) centers coupled to a superoxide radical ($O_2^{\bullet-}$) in either a ferromagnetic or antiferromagnetic manner, respectively.[86] The triplet state arises from antiferromagnetic coupling between a high-spin Fe(II) center and a neutral O_2 ligand. However, we also considered the possibility that the $S = 1$ Fe/O_2 adduct consists of a low-spin Fe(III) ion ferromagnetically coupled to $O_2^{\bullet-}$, as this configuration yielded the lowest-energy Fe/O_2 model in de Visser's study of complex **3**.[39] The resulting computational models are labeled ^{spin}[**2-O₂**]$^{(HS,LS)}$ and ^{spin}[**4-O₂**]$^{(HS,LS)}$, where HS and LS indicate whether the Fe center is high-spin or low-spin, respectively. Metric parameters of the geometry-optimized structures are provided in Table S3. Whereas de Visser found that O_2 binding to **3** triggers dissociation of a pyrazole donor regardless of spin state,[39] nearly all of our optimized Fe/O_2 models are 6C with Fe–$N_{TIP/Tp}$ bond lengths ≤2.31 Å, the only exceptions being the $^{S=3}$[**2-O₂**]^{HS} and $^{S=2}$[**2-O₂**]^{HS} models, in which one of the Fe–N_{TIP} bonds elongates to ~2.4 Å during geometry optimization to yield quasi-6C structures (Table S3).

Table 2 summarizes the computed thermodynamic parameters for the eight Fe(II) + $O_2 \rightarrow$ Fe/O_2 reactions examined here. For both [**2-O₂**] and [**4-O₂**], the four spin states lie within 3 kcal/mol of each other. This result is typical of ferric–superoxo species, which

commonly possess a large number of close-lying electronic states.[86] The enthalpic (ΔH_{rxn}) contributions to O_2 binding are generally insignificant or slightly favorable, yet the overall process is endergonic (ΔG_{rxn} = 8–13 kcal/mol) due to the unfavorable entropic effects characteristic of bimolecular reactions. Although the differences are within the uncertainty of the methodology, the computed ΔG_{rxn}-values are uniformly smaller for the [**4-O₂**] models relative to their [**2-O₂**] counterparts, suggesting that the Tp-based complexes have a higher affinity for O_2 than the TIP-based complexes. This conclusion is supported by the fact that the computed v(O–O) frequencies for the [**4-O₂**] models are 15–25 cm^{-1} lower in energy compared to their counterparts in the analogous [**2-O₂**] models (Table 2), implying that the $^{Ph,Me}Tp^-$ ligand promotes greater charge transfer from Fe(II) to O_2. Analysis of the Mulliken populations revealed that the S-donors in the Fe/O_2 adducts possess a significant amount of spin-density, with alpha-spin-values of 0.33 and 0.27 in the S = 2 structures of [**2-O₂**] amd [**4-O₂**], respectively. This partial radical character, which is consistently larger in the TIP-containing models, likely promotes formation of the S–O bond in the next step of the mechanism.

Table 2. Energetic Parameters Computed for O_2 Binding to Complexes **2** and **4**, and Comparison of Superoxo Stretching Frequencies in the Resulting [FeO₂] Adducts

S_{tot} (Fe spin)[a]	reactants	ΔH_{rxn}	ΔS_{rxn}[b]	ΔG_{rxn}[b]	v(O–O) (cm^{-1})
S = 3 (HS)	**2** + O_2	0.5	10.3	10.8	1222
	4 + O_2	−1.3	10.6	9.3	1197
S = 2 (HS)	**2** + O_2	2.3	10.8	13.1	1213
	4 + O_2	0.7	11.2	11.9	1198
S = 1 (HS)	**2** + O_2	1.7	11.2	12.9	1269
	4 + O_2	−0.3	12.3	12.0	1243
S = 1 (LS)	**2** + O_2	−3.3	14.6	11.3	1183
	4 + O_2	−7.1	15.1	8.0	1160

[a]S_{tot} is the overall spin of the [FeO₂] adduct, whereas HS and LS indicate the spin state of the Fe center itself.
[b]Thermodyanmic parameters were computed assuming a temperature of 298.15 K.

The majority of computational studies of CDO and synthetic mimics suggest that formation of the critical Fe(II)–O–O–S cyclic intermediate occurs along the S = 2 potential energy surface (PES).[39,40,83] Our DFT calculations revealed that conversion of $^{S=2}$[**2-O₂**]^{HS} and $^{S=2}$[**4-O₂**]^{HS} to the corresponding peroxo species occurs with overall transition-state barriers of 25 and 23 kcal/mol, respectively,

relative to the Fe(II) and O_2 starting materials (Scheme 3). The barrier of ~12 kcal/mol for O_d–S bond formation is in line with previous DFT studies of WT CDO and related models, which reported values around 10 kcal/mol for the same mechanistic step.[40,87] The difference in transition-state energies between $^{S=2}$[**2-O₂**]^{HS} and $^{S=2}$[**4-O₂**]^{HS} lies within the estimated error of the computations (±2 kcal/mol), consistent with our experimental finding that the identity of L_{N3} does not have a major impact on dioxygenation rates. Significantly, the computed activation parameters for $^{S=2}$[**2-O₂**]^{HS} ($\Delta H^{\ddagger} = 10.5$ kcal/mol, $\Delta S^{\ddagger} = -48$ cal/(mol·K)) are in reasonably good agreement with the experimentally determined values of $\Delta H^{\ddagger} = 12(1)$ kcal/mol, $\Delta S^{\ddagger} = -25(4)$ cal/(mol·K). In the DFT-optimized transition-state geometry derived from $^{S=2}$[**2-O₂**]^{HS} (Scheme 3), the O–O bond is positioned directly over the Fe–S bond, giving rise to a S···O_d distance of 2.18 Å. The O–O and Fe–S bonds are elongated by 0.040 and 0.212 Å, respectively, compared to the $^{S=2}$[**2-O₂**]^{HS} adduct. The degree of S-radical character in the transition state, as indicated by Mulliken spin populations, is significantly greater for TIP-based **2** (0.18 spins) than Tp-based **4** (0.11 spins). The distribution of unpaired spin density in the transition-state structure (Figure S9) indicates that the S–O_d bond is formed via the overlap between the S-based p_z-orbital and the O_2-based π* orbital oriented along the S–O_d axis.
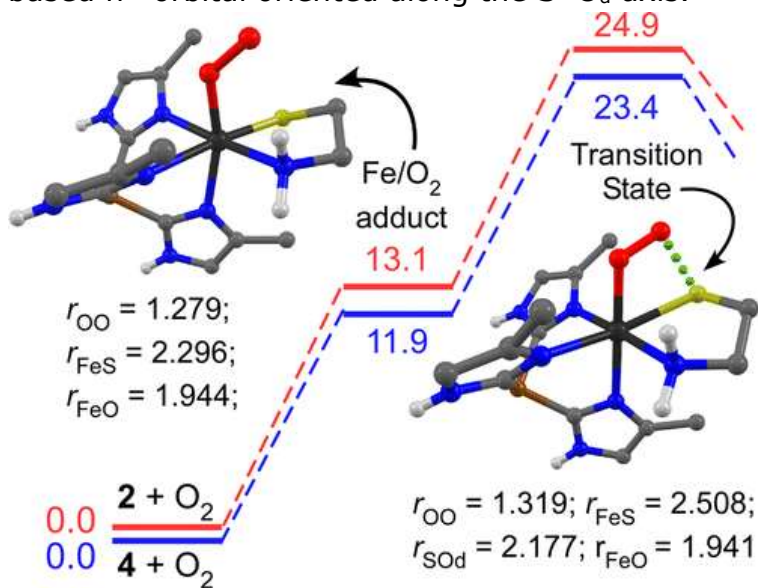
Scheme 3. Relative Energies (in kcal/mol) for the Initial Steps in the Reaction of **2** (Red Lines) and **4** (Blue Lines) with O_2 at 298.15 K[a]

[a]Geometry-optimized structures of $^{S=2}$[**2**-O_2]^{HS} (left) and $^{S=2}$[**2**-O_2]^{TS} (right) are also provided, and select bond lengths are indicated in angstroms (Å).

For the sake of completeness, we also examined the cyclization reaction along the $S = 1$ PES originating from the $^{S=1}$[**2-O₂**]^{LS} and $^{S=1}$[**4-O₂**]^{LS} species, as this process yielded the lowest-energy transition state in de Visser's study of complex **3**.[39] However, the barrier for the $S = 1$ route is nearly 10 kcal/mol higher in energy than the $S = 2$ pathway, suggesting that the former is not a viable option for the dioxygenation mechanism if the Fe center remains six coordinate.

As shown in Figure S10, the energies of the resulting Fe(II)–O–O–S cyclic intermediates on the $S = 2$ PES are roughly equal to those of the preceding Fe/O_2 adducts. The next step in the mechanism requires O–O bond cleavage to yield a high-spin oxoiron(IV) unit bound to a sulfoxide ligand. Our DFT calculations indicate that the transition-state barrier for O–O bond cleavage is quite small (~2 kcal/mol; Figure S10), providing further evidence that formation of the Fe–O–O–S species is the rate-limiting step in the dioxygenation mechanism.

3.6 Nitric Oxide Reactivity: Experimental Results

Using nitric oxide (NO) as a surrogate for O_2 is a common strategy for gaining insights into the electronic structures of ferrous centers in MNIDs and related complexes, since the reaction gives rise to an EPR-active {FeNO}^{7} species (using the Enemark–Feltham notation, where the superscript indicates the sum of Fe 3d and NO π* electrons). A notable feature of CDO is that the enzyme–substrate complex binds NO to yield a low-spin ($S = 1/2$) Fe/NO adduct, as opposed to a high-spin ($S = 3/2$) adduct as is generally observed for MNID enzymes with the 2H1C triad.[88]

Our studies found that exposure of **1** and **2** to NO yields different species depending on the temperature of the reaction. For both complexes, the Fe/NO adducts generated at −70 °C (**1NO** and **2NO**) feature two absorption bands near 440 and 660 nm. As shown in Figure 6, these spectra closely resemble those reported previously for high-spin, six-coordinate (6C) {FeNO}^{7} complexes with similar ligand

sets, such as $[Fe(NO)(4\text{-}TIP^{Ph})(acac)]^+$ and $[Fe(NO)(^{Ph2}Tp)(acac^{PhF3})]$ (where $4\text{-}TIP^{Ph}$ = tris(2-phenylimidazol-4-yl)phosphine and $acac^{PhF3}$ = anion of 4,4,4-trifluoro-1-phenyl-1,3-butanedione; the structure of the latter complex was verified crystallographically).[45] The corresponding X-band EPR spectra (Figure 6; inset) exhibit an axial $S = 3/2$ signal ($g \sim 4.0, 2.0$), also characteristic of 6C $\{FeNO\}^7$ species.[89] The intensity of the $S = 3/2$ signal was measured between 10 and 50 K for **1NO**, and simulation of the data provided a D-value of 6.7(3) cm^{-1} and E/D-ratio of 0.005. We also generated Fe/NO adducts of **3** and **4** (**3NO** and **4NO**, respectively), as Limberg and co-workers did not report NO-binding studies for these complexes. The electronic absorption and EPR data of **3NO** and **4NO** (not shown) are nearly identical to those obtained for **1NO** and **2NO**, indicating that the L_{N3} ligand has little effect on NO reactivity or the spectroscopic features of the resulting species. Therefore, only the iron–nitrosyl adducts derived from **1** and **2** will be discussed in detail.
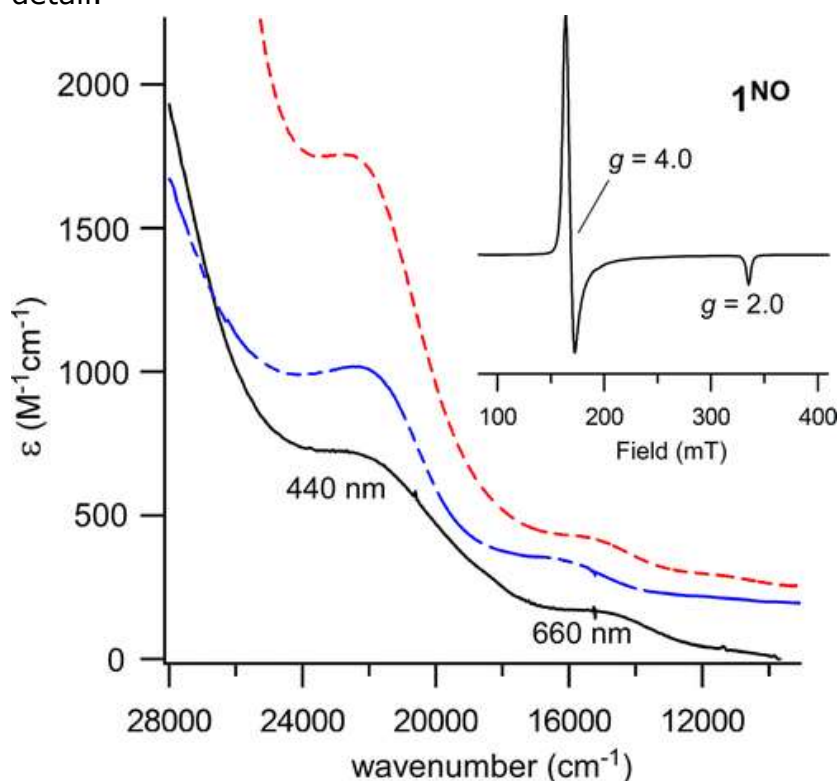
Figure 6. Absorption spectrum of **1NO** (black solid line) generated via reaction of **1** with NO at −70 °C in CH_2Cl_2. Previously reported[45] UV–vis spectra of $[Fe(NO)(4\text{-}TIP^{Ph})(acac)]^+$ (blue dashed line) and $[Fe(NO)(^{Ph2}Tp)(acac^{Ph,F3})]$ in MeCN and CH_2Cl_2, respectively, are shown for comparison (these spectra have been shifted upward for clarity). Inset: X-band EPR spectrum of **1NO** in frozen CH_2Cl_2. Parameters: frequency = 9.380 GHz; power = 2.0 mW; modulation amplitude = 2.0 G; T = 10 K.

In addition to the dominant S = 3/2 resonances arising from **1^NO** and **2^NO**, EPR spectra of samples exposed to NO at low temperatures contained variable amounts of a minor S = 1/2 signal (Figures 7 and S11). The concentrations of the low-spin species, labeled **1^NO-LS** and **2^NO-LS** , were generally less than 10% of total Fe as determined by double integration of the signal at 77 K.[90] Notably, these rhombic spectra exhibit 1:1:1 triplet superhyperfine splitting in each of the three g-values, corresponding to a ^{14}N nucleus with $A_{x,y,z}$ = 36, 37, and 45 MHz in the case of **2^NO-LS** (the complete set of spin-Hamiltonian parameters is provided in Table 3). This pattern converts to a 1:1 doublet when the samples are prepared with ^{15}NO (Figures 7 and S11), confirming that the splitting is due to the N-atom of a *single* NO ligand. Therefore, we can rule out the possibility that the **1^NO-LS** and **2^NO-LS** signals are due to formation of a DNIC. Possible structures for these S = 1/2 species derived from DFT calculations will be discussed in the next section.
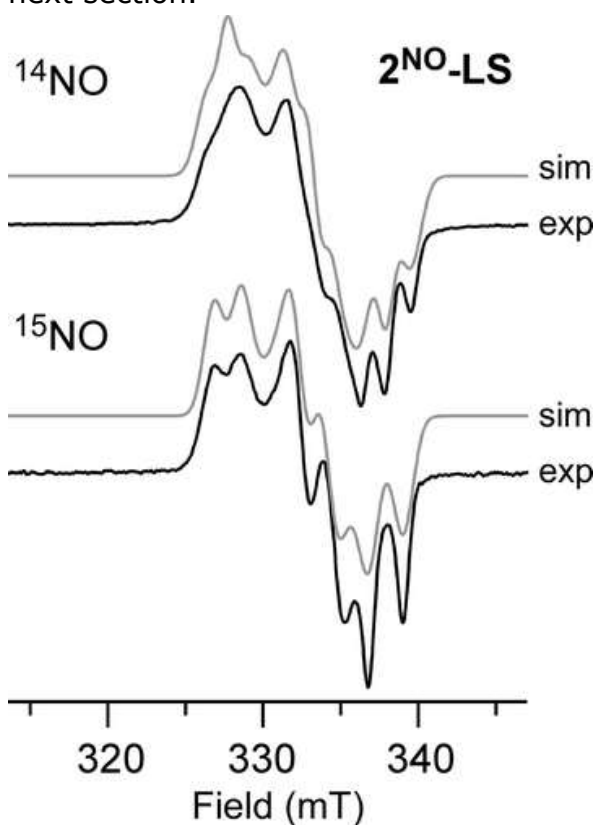
Figure 7. EPR spectra of **2^NO-LS** (black solid line) generated via reaction of **1** with ^{14}NO (top) or ^{15}NO (bottom) at −70 °C in CH_2Cl_2. Parameters: frequency = 9.492 GHz; power = 2.0 mW; modulation amplitude = 1.0 G; T = 77 K. Simulations of the experimental data (gray lines) were generated using the spin-Hamiltonian parameters listed in Table 3.

Table 3. Experimental and Computed EPR Parameters for Low-Spin {FeNO}[7] Species

species	method	g_x	g_y	g_z	A_x	A_y	A_z
					^{14}N A-values (MHz)[a]	
1[NO]-LS	expt	2.009	2.037	2.072	46	41	44
2[NO]-LS	expt	2.007	2.035	2.070	45	37	36
$^{S=1/2}$[**2-NO**]^{6C}	DFT/BP86	1.985	2.014	2.042	43	68	39
	DFT/TPSSh	1.986	2.004	2.022	31	81	36
$^{S=1/2}$[**2-NO**]^{5C}	DFT/BP86	2.005	2.021	2.047	50	46	41
	DFT/TPSSh	2.007	2.031	2.054	53	34	28
[Fe(NO)(N3PyS)]$^+$	expt[b]	1.962	2.007	2.047	40	59	40
6C complex	DFT/BP86	1.976	2.006	2.025	29	62	32
	DFT/TPSSh	1.975	2.001	2.019	19	82	23
Fe(OEP)(NO)	expt[c]	2.015	2.057	2.106	41	50	43
Fe(II)CDO-Cys/NO	expt[d]	1.979	2.028	2.071	<30	100	<30

[a]In most cases, the orientations of the computed **g**- and **A**-tensors did not align. Thus, spectral simulations with the computed Euler angles were used to determine the *A*-value corresponding to each *g*-value.
[b]Reference.[34]
[c]OEP = octaethylporphyrin(2−); refs.[97,99]
[d]Reference.[88]

The reaction of **1** (or **2**) with NO at room temperature (RT) initially generates a chromophore with absorption features matching those observed at −70 °C. However, **1[NO]** and **2[NO]** are not stable at elevated temperatures, quickly converting to the same new species (**RT[NO]**) characterized by a weak absorption band at 910 nm (Figure 8). Time-dependent absorption spectra for this reaction display an isosbestic point at 820 nm, indicating clean conversion of **1[NO]** or **2[NO]** to **RT[NO]** without the buildup of intermediates (Figure S12). EPR spectra collected for frozen solutions of **RT[NO]** exhibit a sharp, rhombic $S = 1/2$ signal that lacks hyperfine splitting (Figure 8, inset), along with a very weak peak at $g = 4.0$ arising from residual **1[NO]** or **2[NO]**. Unfortunately, despite repeated attempts, we were unable to grow crystals of **RT[NO]** suitable for X-ray crystallography.
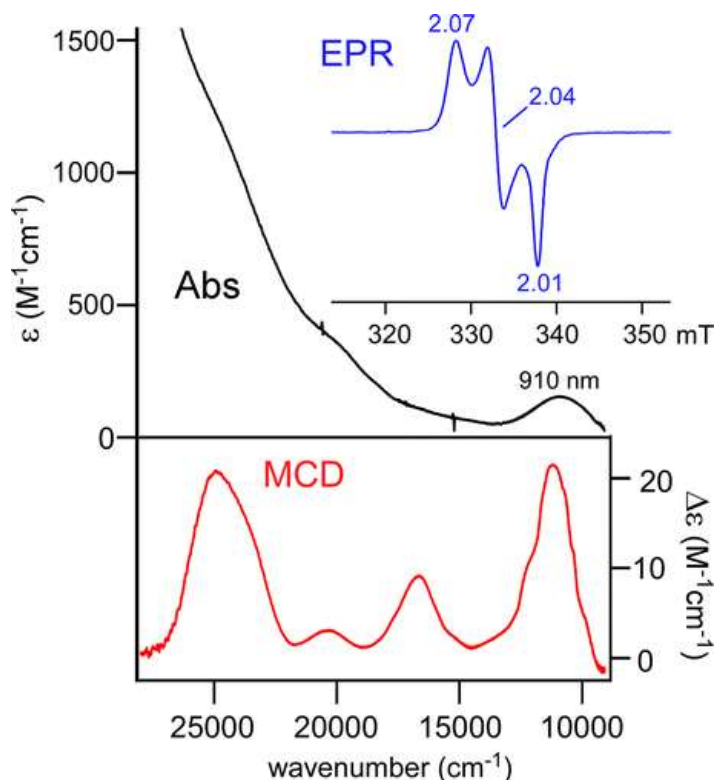
Figure 8. Electronic absorption (top, black) and MCD (bottom, red) spectra of RT^{NO} prepared via reaction of NO with complex **1** at ambient temperature. The absorption spectrum was measured in CH_2Cl_2. The MCD spectrum was obtained for a frozen, glassy solution in 1:1 (v/v) CH_2Cl_2:butyronitrile at a temperature of 4 K and a magnetic field of 7 T. Inset: X-band EPR spectrum (blue line) of RT^{NO} in frozen CH_2Cl_2. Parameters: frequency = 9.497 GHz; power = 0.5 mW; modulation amplitude = 1.0 G; T = 77 K.

  Notably, the absorption and EPR features of **RT^{NO}** are quite similar to those reported for cationic, dinitrosyl iron complexes (DNICs) with the general formula $[Fe(NO)_2(L_{N2})]^+$ (where L_{N2} is a neutral *N,N*-donor).[91-94] Like **RT^{NO}**, these $S = 1/2$ $\{Fe(NO)_2\}^9$ species commonly exhibit a rhombic **g**-tensor centered at 2.03 and a broad absorption band in the near-IR region with an extinction coefficient of ~100 M^{-1} cm^{-1}. To determine whether **RT^{NO}** corresponds to a DNIC, IR spectra of NO-treated **1** and **2** were measured at RT. The resulting spectra display two intense peaks at 1745 and 1817 cm^{-1}, both of which downshift by ~34 cm^{-1} upon ^{15}NO substitution (Figure S13). These frequencies and isotope shifts are consistent with prior studies of $[Fe(NO)_2(L_{N2})]^+$ complexes, which revealed that the out-of-phase and in-phase combinations of v(NO) modes occur within energy ranges of 1720–1770 and 1790–1840 cm^{-1}, respectively. Furthermore, the separation between NO stretching frequencies (Δv_{NO}) is diagnostic of

coordination number and nuclearity,[95] and the $\Delta\nu_{NO}$-value of 72 cm^{-1} measured for **RT^{NO}** is typical of four-coordinate (4C) $\{Fe(NO)_2\}^9$ species.[91-94]

The formation of $\{Fe(NO)_2\}^9$ DNICs from Fe(II)–thiolate precursors requires formation of 0.5 equiv of disulfide to provide the additional electron. Analysis with GC–MS found that l-cystine ethyl ester was the only CysOEt-derived product generated during the **1** + NO reaction at RT. Thus, our collective experimental results suggest that DNIC formation occurs via the reaction

$$[Fe(NO)(^{Ph2}TIP)(CysOEt)]^+(\mathbf{1^{NO}}) + NO \rightarrow [Fe(NO)_2(^{Ph2}TIP)]^+(\mathbf{RT^{NO}}) + \frac{1}{2}RS-SR$$
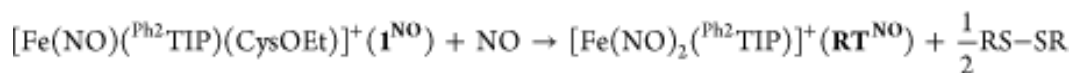
where R = $-CH_2CH(NH_2)CO_2Et$. This conclusion is supported by the fact that the spectroscopic parameters of **RT^{NO}** are identical regardless of whether **1** or **2** serves as the precursor, indicating that the thiolate ligand is no longer attached to the iron-containing product.

To further probe the electronic properties of **RT^{NO}**, we collected MCD spectra for frozen solutions in 1:1 (v/v) CH_2Cl_2:butyronitrile. Whereas the absorption spectrum of **RT^{NO}** exhibits few well-defined features, the MCD spectrum measured at 4 K and 7 T shows four distinct bands between 10,000 and 25,000 cm^{-1} (Figure 8). Variable-temperature variable-field (VTVH) MCD data collected at 907 nm (Figure S14) confirm that the MCD bands arise from a $S = 1/2$ species, consistent with the EPR results. To the best of our knowledge, these data represent the first MCD analysis of a DNIC. The origins of the observed absorption/MCD features were elucidated with the help of TD-DFT calculations, as discussed in the following section.

3.7 Nitric Oxide Reactivity: Computational Results

DFT calculations for Fe/NO species derived from complexes **1** and **2** utilized either the nonhybrid BP86 or hybrid meta-GGA TPSSh functionals, which are known to provide accurate geometries and spectroscopic parameters for both mono- and dinitrosyl iron complexes.[94] Geometry optimizations of the high-spin $\{FeNO\}^7$ adduct obtained upon NO binding to **2** yielded quasi-6C structures, labeled

$S=3/2$[**2-NO**]^{6C}, with an elongated distance of 2.5 Å for the Fe–N$_{TIP}$ bond *trans* to the nitrosyl (Table S4), indicative of the strong *trans* influence of NO ligands.[96] Interestingly, during the BP86 geometry optimizations of the low-spin {FeNO}^{7} adduct, the *trans* imidazole fully dissociated and formed an intramolecular H-bond with the amine group of CysAm, yielding the 5C structure $S=1/2$[**2-NO**]^{5C}. In order to generate a low-spin 6C model (i.e., $S=1/2$[**2-NO**]^{6C}), it was necessary to constrain the *trans* Fe–N$_{TIP}$ bond distance to 2.3 Å. The structures and relative energies of the three BP86-optimized models are provided in Figure 9. The $S=1/2$[**2-NO**]^{5C} structure is more stable than both $S=3/2$[**2-NO**]^{6C} and $S=1/2$[**2-NO**]^{6C} by several kcal/mol. When the TPSSh functional is employed instead of BP86, a low-spin {FeNO}^{7} species with a quasi-6C structure (*trans* Fe–N$_{TIP}$ distance of 2.41 Å) was found to exist in a local minimum. While the three TPSSh-generated structures are fairly close in energy, the $S=1/2$[**2-NO**]^{5C} structure remains the most stable (Figure 9).
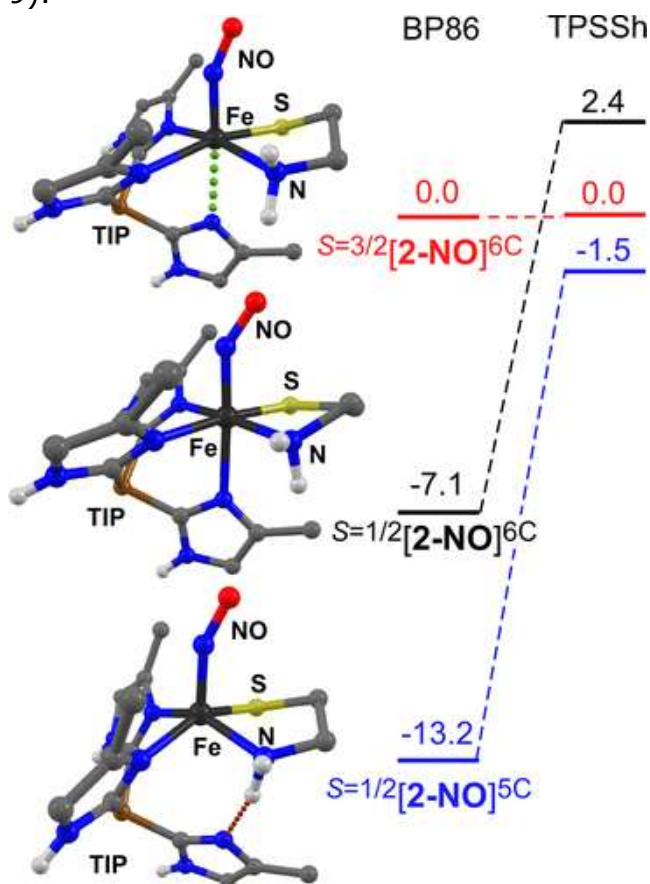
Figure 9. DFT optimized structures and relative energies (in kcal/mol) of the $S=3/2$[**2**-NO]^{6C}, $S=1/2$[**2**-NO]^{6C}, and $S=1/2$[**2**-NO]^{5C} models computed using the BP86 and TPSSh functionals. The structures were derived from the BP86 calculations.

To determine whether the $^{S=1/2}$[**2-NO**]^{5C} structure corresponds to the mononitrosyl $S = 1/2$ species observed via EPR spectroscopy (Figure 7), we calculated g-values and ^{14}N **A**-tensors using both functionals. We also performed parallel calculations for [Fe(NO)(N3PyS)]$^+$, a structurally characterized 6C, low-spin {FeNO}^{7} complex prepared by Goldberg and co-workers.[34] As shown in Table 3, our DFT methodology accurately reproduces the EPR features of this complex, namely, its rhombic **g**-tensor centered near g_e = 2.00 and large A_y-value. Importantly, the calculations are consistent with prior studies of low-spin {FeNO}^{7} complexes, both heme and non-heme, which have revealed that certain spin-Hamiltonian parameters are diagnostic of coordination number.[97-100] Specifically, the g_x-values of 6C species are always less than the free-electron value (g_e = 2.002), whereas $g_x > g_e$ for 5C {FeNO}^{7} species. Additionally, the **A**-tensors of 6C complexes exhibit relatively large anisotropy and a dominant A_y-value, whereas 5C complexes possess relatively isotropic ^{14}N **A**-tensors in which the A_x-value is the largest component (Table 3). The EPR parameters of **1NO-LS** and **2NO-LS** closely align with those computed for $^{S=1/2}$[**2-NO**]^{5C}, as well as those observed for 5C NO adducts of ferrous–porphyrin complexes.[97-100] Thus, we conclude that the observed low-spin signal is due to dissociation of the *trans* imidazole donor in a fraction of the {FeNO}^{7} adducts prepared at low temperature.

We also generated computational models with the formula [Fe(NO)$_2$(^{Me}TIP)]$^+$ to further confirm that **RT^{NO}** corresponds to a cationic DNIC. These calculations employed the broken-symmetry approach to generate the proper $S = 1/2$ wave function, best described as a high-spin Fe(III) center coupled antiferromagnetically to two NO$^-$ ($S = 1$) ligands.[101] Regardless of the functional used, geometry optimizations of the **DNIC^{DFT}** models converged to four-coordinate (4C) structures with a κ^2-TIP ligand, further demonstrating the hemilability of the TIP framework. The computed spectroscopic properties of the **DNIC^{DFT}** models are summarized in Table 4. DFT is known to overestimate v(NO) frequencies, with hybrid functionals generally performing worse than nonhybrid functionals.[94,101] While our results follow this pattern, the BP86 functional proved quite effective in estimating the energy splitting between the in-phase and out-of-phase

combinations of v(NO) modes of **RT^{NO}**. Both functionals yielded rhombic **g**-tensors centered near $g = 2.03$, consistent with our EPR data and prior studies of DNICs.[91-94] The computed **A**-tensors are highly anisotropic with two small *A*-values (<10 MHz) and one moderate value of 25 or 39 MHz, in accordance with the absence of any detectable ^{14}N hyperfine splitting in the experimental **RT^{NO}** EPR spectrum.

Table 4. Comparison of Computed Spectroscopic Parameters for **DNIC^{DFT}** Models with Experimental Values Measured for **RT^{NO}**

	DNIC^{DFT} (BP86)	**DNIC^{DFT} (TPSSh)**	**RT^{NO} (expt)**
v(NO)$_{sym}$, v(NO)$_{asym}$	1843, 1776 cm^{-1}	1897, 1816 cm^{-1}	1817, 1745 cm^{-1}
g_x, g_y, g_z	2.013, 2.028, 2.058	2.027, 2.033, 2.061	2.01, 2.04, 2.07
A_x, A_y, A_z (^{14}N7)	3, 22, 3 MHz	7, 36, 13 MHz	not observed
A_x, A_y, A_z (^{14}N8)	4, 5, 25 MHz	1, 8, 39 MHz	

Consistent with the experimental absorption spectrum of **RT^{NO}**, TD-DFT calculations of **DNIC^{DFT}** predict a series of weak bands (ε-values < 400 M^{-1} cm^{-1}) in the visible region (Figure S15). The donor MOs for these transitions contain approximately equal amounts of Fe 3d and NO π* character due to the highly covalent nature of the iron–nitrosyl bonds. In contrast, the acceptor orbital is the Fe(d$_{x^2-y^2}$)-based MO that lies in the N$_{TIP}$–Fe–N$_{TIP}$ plane and lacks contributions from the NO ligands (Figure S15). Thus, the transitions have both ligand-field and NO$^-$ → Fe(III) CT character, but their intensities are limited by the poor spatial overlap between donor and acceptor MOs.

4 Conclusions

The syntheses, X-ray crystallographic structures, electronic properties, and O$_2$/NO reactivities of two novel TDO active-site models (**1** and **2**) have been reported. These 5C Fe(II) complexes consist of a bidentate "substrate" ligand (CysOEt or CysAm) and the facially coordinating ^{Ph2}TIP supporting ligand (Scheme 2). In our estimation, **1** and **2** are the most structurally accurate models of the CDO and ADO active sites prepared to date, as the ^{Ph2}TIP supporting ligand reproduces the neutral charge and all-imidazole coordination of the 3His triad. The electronic structures of **1** and **2**, along with those of the previously reported ^{Ph,Me}Tp-based TDO models (**3** and **4**), were elucidated with spectroscopic (absorption, MCD) and computational

(DFT) techniques. These studies yielded specific assignments for the three overlapping S → Fe(II) CT transitions in the near-UV region, and MCD analysis permitted observation of the highest-energy d–d transition at ~11,300 cm^{-1}. In addition, they revealed that substitution of neutral ^{Ph2}TIP with anionic $^{Ph,Me}Tp^-$ destabilizes the Fe 3d manifold by ~0.13 eV and significantly reduces the covalency of the Fe–S bond.

Like similar complexes generated by the Limberg and Goldberg groups, **1** and **2** are functional TDO mimics that react with O_2 to yield the corresponding sulfinic acid product. Our kinetic studies determined that the identity of the L_{N3} ligand (^{Ph2}TIP versus $^{Ph,Me}Tp^-$) has little effect on O_2 reaction rates. DFT methods were then employed to evaluate the energetics of formation of the Fe/O_2 adduct and its conversion to the cyclic Fe–O–O-S intermediate; the latter reaction is the putative rate-determining step in the dioxygenation mechanism. These calculations indicated that O_2 binding to the high-spin Fe(II) centers of **2** and **4** is endergonic by 9–13 kcal/mol due to an unfavorable entropic contribution. The transition state leading to the putative Fe–O–O–S intermediate along the $S = 2$ surface is further uphill by ~12 kcal/mol for **2** and **4**, resulting in an overall barrier of ~24 kcal/mol relative to the starting complexes and O_2 (Scheme 3). These computed values are roughly consistent with the experimental activation parameters of $\Delta H^{\ddagger} = 12(1)$ kcal/mol and $\Delta S^{\ddagger} = -25(4)$ cal/(mol·K) measured experimentally for the reaction of **1** with O_2. In both the Fe/O_2 adducts and transition-state structures, the charge of the supporting ligand modulates the amount of unpaired spin density on the S atom of the thiolate ligand, with the TIP-based models exhibiting greater S-radical character than the Tp-based models. This correlation offers a possible rationale for the preference of TDOs for the 3His triad instead of the 2H1C triad, since the development of (partial) thiyl radical character is thought to facilitate formation of the critical Fe–O–O–S species in the enzymatic mechanism.[102]

Since our efforts to trap intermediates in the dioxygenation reactions were unsuccessful, we explored the reactivity of **1** and **2** with NO, an established proxy for O_2. As summarized in Scheme 4, initial NO binding generates a 6C, high-spin {FeNO}^{7} adduct (**1NO** and **2NO**) that is metastable at reduced temperatures, but converts at RT to a more stable 4C DNIC (**RT^{NO}**) with concomitant formation of disulfide.

Samples prepared at low temperatures also revealed a minor $S = 1/2$ signal (**1^{NO}-LS** and **2^{NO}-LS**) that was shown, through a combination of spectroscopic and computational analysis, to correspond to a 5C species featuring a κ^2-TIP ligand. The dissociation of the *trans* imidazole donor may be required for the conversion of the 6C {FeNO}^{7} adducts into the 4C {Fe(NO)$_2$}^{9} species.
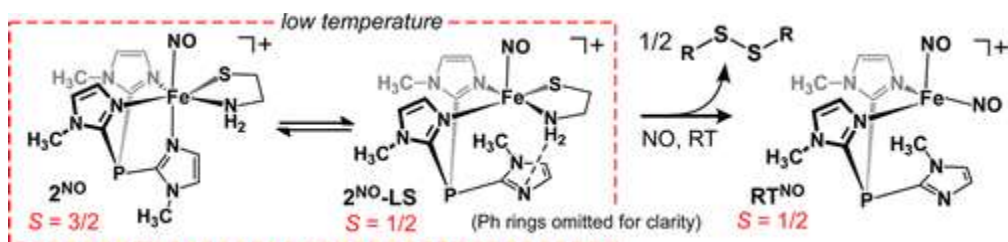
Scheme 4

Interestingly, even though the first-sphere coordination geometries of **1** and **2** are nearly identical to those of CDO and ADO, there are dramatic differences in electronic structure, spectroscopic properties, and reactivity between the synthetic models and enzyme active sites. For example, the S → Fe(II) CT transitions observed for CDO are much higher in energy than those observed for complexes **1**–**4**. In addition, whereas **1^{NO}** and **2^{NO}** are high-spin and decompose at RT to form a DNIC, the 6C {FeNO}^{7} adduct of CDO is low-spin and relatively stable.[88] These differences highlight the importance of the protein environment in fine-tuning the geometric and electronic structures of the non-heme iron active site. The rotational freedom of the imidazolyl and pyrazolyl donors allows the ^{Ph2}TIP and ^{Ph,Me}Tp ligands to adopt κ^2-*N,N* binding modes, thereby encouraging the formation of 5C and 4C Fe/NO adducts. In contrast, QM/MM studies have determined that the binding of NO to substrate-bound CDO causes little change in Fe–N$_{His}$ bond distances,[102] suggesting that the positions of the His ligands are fixed within the active site. Thus, despite the considerable advantages of scorpionate ligands, our future TDO modeling studies will employ more constrained ligands that prevent elongation or breaking of the Fe–N bond *trans* to the O$_2$/NO binding site. Moreover, the incorporation of second-sphere donors capable of hydrogen-bonding interactions would serve to modulate spectroscopic features and stabilize reactive intermediates in a manner similar to the protein environment.

The authors declare no competing financial interest.

Acknowledgment

References

[1]Solomon, E. I.; Brunold, T. C.; Davis, M. I.; Kemsley, J. N.; Lee, S. K.; Lehnert, N.; Neese, F.; Skulan, A. J.; Yang, Y. S.; Zhou, J.Geometric and electronic structure/function correlations in non-heme iron enzymes *Chem. Rev.* 2000, 100, 235– 349, DOI: 10.1021/cr9900275

[2]Costas, M.; Mehn, M. P.; Jensen, M. P.; Que, L.Dioxygen activation at mononuclear nonheme iron active sites: Enzymes, models, and intermediates *Chem. Rev.* 2004, 104, 939– 986, DOI: 10.1021/cr020628n

[3]Vaillancourt, F. H.; Bolin, J. T.; Eltis, L. D.The ins and outs of ring-cleaving dioxygenases *Crit. Rev. Biochem. Mol. Biol.* 2006, 41, 241– 267, DOI: 10.1080/10409230600817422

[4]Parales, R. E.; Haddock, J. D.Biocatalytic degradation of pollutants *Curr. Opin. Biotechnol*. 2004, 15, 374– 379, DOI: 10.1016/j.copbio.2004.06.003

[5]Lipscomb, J. D.Mechanism of extradiol aromatic ring-cleaving dioxygenases *Curr. Opin. Struct. Biol.* 2008, 18, 644– 649, DOI: 10.1016/j.sbi.2008.11.001

[6]Stipanuk, M. H.; Simmons, C. R.; Andrew Karplus, P.; Dominy, J. E., Jr.Thiol dioxygenases: unique families of cupin proteins Amino Acids 2011, 41, 91– 102, DOI: 10.1007/s00726-010-0518-2

[7]Joseph, C. A.; Maroney, M. J.Cysteine dioxygenase: structure and mechanism *Chem. Commun*. 2007, 3338– 3349, DOI: 10.1039/b702158e

[8]Yamaguchi, K.; Hosokawa, Y. Cysteine dioxygenase *Methods Enzymol.* 1987, 143, 395– 403, DOI: 10.1016/0076-6879(87)43069-3

[9]Stipanuk, M. H.; Ueki, I.Dealing with methionine/homocysteine sulfur: cysteine metabolism to taurine and inorganic sulfur *J. Inherited Metab. Dis.* 2011, 34, 17– 32, DOI: 10.1007/s10545-009-9006-9

[10]Ueki, I.; Roman, H. B.; Valli, A.; Fieselmann, K.; Lam, J.; Peters, R.; Hirschberger, L. L.; Stipanuk, M. H.Knockout of the murine cysteine dioxygenase gene results in severe impairment in ability to synthesize

taurine and an increased catabolism of cysteine to hydrogen sulfide *Am. J. Physiol.* 2011, 301, E668– E684, DOI: 10.1152/ajpendo.00151.2011

[11]Slivka, A.; Cohen, G.Brain ischemia markedly elevates levels of the neurotoxic amino acid, cysteine *Brain Res.* 1993, 608, 33– 7, DOI: 10.1016/0006-8993(93)90770-N

[12]Pean, A. R.; Parsons, R. B.; Waring, R. H.; Williams, A. C.; Ramsden, D. B.Toxicity of sulfur-containing compounds to neuronal cell lines *J. Neurol. Sci.* 1995, 129, 107– 8, DOI: 10.1016/0022-510X(95)00078-G

[13]Heafield, M. T.; Fearn, S.; Steventon, G. B.; Waring, R. H.; Williams, A. C.; Sturman, S. G.Plasma cysteine and sulphate levels in patients with motor neurone, Parkinson's and Alzheimer's disease *Neurosci. Lett.* 1990, 110, 216– 20, DOI: 10.1016/0304-3940(90)90814-P

[14]Perry, T. L.; Norman, M. G.; Yong, V. W.; Whiting, S.; Crichton, J. U.; Hansen, S.; Kish, S. J.Hallervorden-Spatz disease: cysteine accumulation and cysteine dioxygenase deficiency in the globus pallidus *Ann. Neurol.* 1985, 18, 482– 9, DOI: 10.1002/ana.410180411

[15]Bradley, H.; Gough, A.; Sokhi, R. S.; Hassell, A.; Waring, R.; Emery, P.Sulfate metabolism is abnormal in patients with rheumatoid arthritis. Confirmation by in vivo biochemical findings *J. Rheumatol*. 1994, 21, 1192– 6

[16]Emery, P.; Bradley, H.; Gough, A.; Arthur, V.; Jubb, R.; Waring, R.Increased prevalence of poor sulphoxidation in patients with rheumatoid arthritis: effect of changes in the acute phase response and second line drug treatment *Ann. Rheum. Dis.* 1992, 51, 318– 20, DOI: 10.1136/ard.51.3.318

[17]Dominy, J. E., Jr.; Simmons, C. R.; Hirschberger, L. L.; Hwang, J.; Coloso, R. M.; Stipanuk, M. H.Discovery and Characterization of a Second Mammalian Thiol Dioxygenase, Cysteamine Dioxygenase *J. Biol. Chem.* 2007, 282, 25189– 25198, DOI: 10.1074/jbc.M703089200

[18]Bruijnincx, P. C. A.; van Koten, G.; Gebbink, R. J. M. K.Mononuclear non-heme iron enzymes with the 2-His-1-carboxylate facial triad: recent developments in enzymology and modeling studies *Chem. Soc. Rev.* 2008, 37, 2716– 2744, DOI: 10.1039/b707179p

[19]Koehntop, K. D.; Emerson, J. P.; Que, L.The 2-His-1-carboxylate facial triad: a versatile platform for dioxygen activation by mononuclear non-heme iron(II) enzymes *JBIC, J. Biol. Inorg. Chem*. 2005, 10, 87– 93, DOI: 10.1007/s00775-005-0624-x

[20]McCoy, J. G.; Bailey, L. J.; Bitto, E.; Bingman, C. A.; Aceti, D. J.; Fox, B. G.; Phillips, G. N., Jr.Structure and mechanism of mouse cysteine dioxygenase *Proc. Natl. Acad. Sci. U. S. A.* 2006, 103, 3084– 3089, DOI: 10.1073/pnas.0509262103

[21]Simmons, C. R.; Liu, Q.; Huang, Q. Q.; Hao, Q.; Begley, T. P.; Karplus, P. A.; Stipanuk, M. H.Crystal structure of mammalian cysteine dioxygenase - A novel mononuclear iron center for cysteine thiol oxidation *J. Biol. Chem.* 2006, 281, 18723– 18733, DOI: 10.1074/jbc.M601555200

[22]Ye, S.; Wu, X. a.; Wei, L.; Tang, D.; Sun, P.; Bartlam, M.; Rao, Z.An Insight into the Mechanism of Human Cysteine Dioxygenase. Key Roles of the Thioether-Bonded Tyrosine-Cysteine Cofactor *J. Biol. Chem.* 2007, 282, 3391– 3402, DOI: 10.1074/jbc.M609337200

[23]Diebold, A. R.; Neidig, M. L.; Moran, G. R.; Straganz, G. D.; Solomon, E. I.The Three-His Triad in Dke1: Comparisons to the Classical Facial Triad *Biochemistry* 2010, 49, 6945– 6952, DOI: 10.1021/bi100892w

[24]Leitgeb, S.; Straganz, G. D.; Nidetzky, B.Biochemical characterization and mutational analysis of the mononuclear non-haem Fe^{2+} site in Dke1, a cupin-type dioxygenase from Acinetobacter johnsonii *Biochem*. J. 2009, 418, 403– 411, DOI: 10.1042/BJ20081161

[25]Leitgeb, S.; Nidetzky, B.Structural and functional comparison of 2-His-1-carboxylate and 3-His metallocentres in non-haem iron(II)-dependent enzymes *Biochem. Soc. Trans.* 2008, 36, 1180– 1186, DOI: 10.1042/BST0361180

[26]Chen, J.; Li, W.; Wang, M.; Zhu, G.; Liu, D.; Sun, F.; Hao, N.; Li, X.; Rao, Z.; Zhang, X. C.Crystal structure and mutagenic analysis of GDOsp, a gentisate 1,2-dioxygenase from Silicibacter Pomeroyi *Protein Sci.* 2008, 17, 1362– 1373, DOI: 10.1110/ps.035881.108

[27]Matera, I.; Ferraroni, M.; Buerger, S.; Scozzafava, A.; Stolz, A.; Briganti, F.Salicylate 1,2-dioxygenase from Pseudaminobacter salicylatoxidans: Crystal structure of a peculiar ring-cleaving dioxygenase *J. Mol. Biol.* 2008, 380, 856– 868, DOI: 10.1016/j.jmb.2008.05.041

[28]Buongiorno, D.; Straganz, G. D.Structure and function of atypically coordinated enzymatic mononuclear non-heme-Fe(II) centers *Coord. Chem. Rev.* 2013, 257, 541– 563, DOI: 10.1016/j.ccr.2012.04.028

[29]Badiei, Y. M.; Siegler, M. A.; Goldberg, D. P.O2 Activation by Bis(imino)pyridine Iron(II)-Thiolate Complexes *J. Am. Chem. Soc.* 2011, 133, 1274– 1277, DOI: 10.1021/ja109923a

[30]Jiang, Y.; Widger, L. R.; Kasper, G. D.; Siegler, M. A.; Goldberg, D. P.Iron(II)-Thiolate S-Oxygenation by O2: Synthetic Models of Cysteine Dioxygenase *J. Am. Chem. Soc.* 2010, 132, 12214– 12215, DOI: 10.1021/ja105591q

[31]McQuilken, A. C.; Goldberg, D. P.Sulfur oxygenation in biomimetic non-heme iron-thiolate complexes *Dalton Trans.* 2012, 41, 10883– 10899, DOI: 10.1039/c2dt30806a

[32]Widger, L. R.; Jiang, Y.; Siegler, M. A.; Kumar, D.; Latifi, R.; de Visser, S. P.; Jameson, G. N. L.; Goldberg, D. P.Synthesis and Ligand Non-

Innocence of Thiolate-Ligated (N4S) Iron(II) and Nickel(II) Bis(imino)pyridine Complexes *Inorg. Chem*. 2013, 52, 10467– 10480, DOI: 10.1021/ic4013558

[33]McQuilken, A. C.; Jiang, Y.; Siegler, M. A.; Goldberg, D. P.Addition of Dioxygen to an N4S(thiolate) Iron(II) Cysteine Dioxygenase Model Gives a Structurally Characterized Sulfinato-Iron(II) Complex *J. Am. Chem. Soc.* 2012, 134, 8758– 8761, DOI: 10.1021/ja302112y

[34]McQuilken, A. C.; Ha, Y.; Sutherlin, K. D.; Siegler, M. A.; Hodgson, K. O.; Hedman, B.; Solomon, E. I.; Jameson, G. N. L.; Goldberg, D. P.Preparation of Non-heme {FeNO}[7] Models of Cysteine Dioxygenase: Sulfur versus Nitrogen Ligation and Photorelease of Nitric Oxide *J. Am. Chem. Soc.* 2013, 135, 14024– 14027, DOI: 10.1021/ja4064487

[35]McQuilken, A. C.; Matsumura, H.; Durr, M.; Confer, A. M.; Sheckelton, J. P.; Siegler, M. A.; McQueen, T. M.; Ivanovic-Burmazovic, I.; Moenne-Loccoz, P.; Goldberg, D. P.Photoinitiated Reactivity of a Thiolate-Ligated, Spin-Crossover Nonheme {FeNO}[7] Complex with Dioxygen *J. Am. Chem. Soc.* 2016, 138, 3107– 3117, DOI: 10.1021/jacs.5b12741

[36]Sallmann, M.; Siewert, I.; Fohlmeister, L.; Limberg, C.; Knispel, C.A Trispyrazolylborato Iron Cysteinato Complex as a Functional Model for the Cysteine Dioxygenase *Angew. Chem., Int. Ed.* 2012, 51, 2234– 2237, DOI: 10.1002/anie.201107345

[37]Sallmann, M.; Braun, B.; Limberg, C.Dioxygenation of cysteamine to hypotaurine at a tris(pyrazolyl)borate iron(II) unit - cysteamine dioxygenase mimicking? *Chem. Commun.* 2015, 51, 6785– 6787, DOI: 10.1039/C5CC01083G

[38]Sallmann, M.; Limberg, C.Utilizing the trispyrazolyl borate ligand for the mimicking of O_2-activating mononuclear nonheme iron enzymes *Acc. Chem. Res.* 2015, 48, 2734– 2743, DOI: 10.1021/acs.accounts.5b00148

[39]Sallmann, M.; Kumar, S.; Chernev, P.; Nehrkorn, J.; Schnegg, A.; Kumar, D.; Dau, H.; Limberg, C.; de Visser, S. P.Structure and mechanism leading to formation of the cysteine sulfinate product complex of a biomimetic cysteine dioxygenase model *Chem. - Eur. J.* 2015, 21, 7470– 7479, DOI: 10.1002/chem.201500644

[40]Kumar, D.; Sastry, G. N.; Goldberg, D. P.; de Visser, S. P.Mechanism of S-Oxygenation by a Cysteine Dioxygenase Model Complex *J. Phys. Chem. A* 2012, 116, 582– 591, DOI: 10.1021/jp208230g

[41]Gonzalez-Ovalle, L. E.; Quesne, M. G.; Kumar, D.; Goldberg, D. P.; de Visser, S. P.Axial and equatorial ligand effects on biomimetic cysteine dioxygenase model complexes *Org. Biomol. Chem.* 2012, 10, 5401– 5409, DOI: 10.1039/c2ob25406a

[42]Alberto, M. E.A trispyrazolylborato iron cysteinato complex efficiently mimics the cysteine dioxygenation process: mechanistic insights *Chem. Commun*. 2015, 51, 8369– 8372, DOI: 10.1039/C5CC00813A

[43]Park, H.; Baus, J. S.; Lindeman, S. V.; Fiedler, A. T.Synthesis and Characterization of Fe(II) beta-Diketonato Complexes with Relevance to Acetylacetone Dioxygenase: Insights into the Electronic Properties of the 3-Histidine Facial Triad *Inorg. Chem.* 2011, 50, 11978– 11989, DOI: 10.1021/ic201115s

[44]Bittner, M. M.; Baus, J. S.; Lindeman, S. V.; Fiedler, A. T.Synthesis and Structural Characterization of Iron(II) Complexes with Tris(imidazolyl)phosphane Ligands: A Platform for Modeling the 3-Histidine Facial Triad of Nonheme Iron Dioxygenases *Eur. J. Inorg. Chem.* 2012, 2012, 1848– 1856, DOI: 10.1002/ejic.201101282

[45]Park, H.; Bittner, M. M.; Baus, J. S.; Lindeman, S. V.; Fiedler, A. T.Fe(II) Complexes That Mimic the Active Site Structure of Acetylacetone Dioxygenase: O_2 and NO Reactivity *Inorg. Chem.* 2012, 51, 10279– 10289, DOI: 10.1021/ic3012712

[46]Baum, A. E.; Lindeman, S. V.; Fiedler, A. T.Mononuclear Iron-(hydro/semi)-quinonate Complexes Featuring Neutral and Charged Scorpionates: Synthetic Models of Intermediates in the Hydroquinone Dioxygenase Mechanism *Eur. J. Inorg. Chem.* 2016, 2016, 2455– 2464, DOI: 10.1002/ejic.201501380

[47]Smith, A. T.; Majtan, T.; Freeman, K. M.; Su, Y.; Kraus, J. P.; Burstyn, J. N.Cobalt Cystathionine β-Synthase: A Cobalt-Substituted Heme Protein with a Unique Thiolate Ligation Motif *Inorg. Chem*. 2011, 50, 4417– 4427, DOI: 10.1021/ic102586b

[48]Tietz, T.; Limberg, C.; Stoesser, R.; Ziemer, B.Four-Coordinate Trispyrazolyl-boratomanganese and -iron Complexes with a Pyrazolato Co-ligand: Syntheses and Properties as Oxidation Catalysts *Chem. - Eur. J.* 2011, 17, 10010– 10020, DOI: 10.1002/chem.201100343

[49]Stoll, S.; Schweiger, A.EasySpin, a comprehensive software package for spectral simulation and analysis in EPR *J. Magn. Reson.* 2006, 178, 42– 55, DOI: 10.1016/j.jmr.2005.08.013

[50]Sheldrick, G. M.A short history of SHELX *Acta Crystallogr., Sect. A: Found. Crystallogr.* 2008, 64, 112– 122, DOI: 10.1107/S0108767307043930

[51]Dolomanov, O. V.; Bourhis, L. J.; Gildea, R. J.; Howard, J. A. K.; Puschmann, H.OLEX2: a complete structure solution, refinement and analysis program *J. Appl. Crystallogr.* 2009, 42, 339– 341, DOI: 10.1107/S0021889808042726

[52]Kryatov, S. V.; Rybak-Akimova, E. V.; Schindler, S.Kinetics and Mechanisms of Formation and Reactivity of Non-heme Iron Oxygen Intermediates *Chem. Rev.* 2005, 105, 2175– 2226, DOI: 10.1021/cr030709z

[53]Battino, R.; Clever, H. L.Solubility of gases in liquids *Chem. Rev.* 1966, 66, 395– 463, DOI: 10.1021/cr60242a003

[54]Neese, F. *ORCA - An Ab Initio, DFT and Semiempirical Electronic Structure Package, version 3.0;* Max Planck Institute for Chemical Energy Conversion: Muelheim, Germany, 2013.

[55]Schafer, A.; Huber, C.; Ahlrichs, R.Fully Optimized Contracted Gaussian-Basis Sets of Triple Zeta Valence Quality for Atoms Li to Kr *J. Chem. Phys.* 1994, 100, 5829– 5835, DOI: 10.1063/1.467146

[56]Schafer, A.; Horn, H.; Ahlrichs, R.Fully Optimized Contracted Gaussian-Basis Sets for Atoms Li to Kr *J. Chem. Phys.* 1992, 97, 2571– 2577, DOI: 10.1063/1.463096

[57]Weigend, F.; Ahlrichs, R.Balanced basis sets of split valence, triple zeta valence and quadruple zeta valence quality for H to Rn: Design and assessment of accuracy *Phys. Chem. Chem. Phys.* 2005, 7, 3297– 3305, DOI: 10.1039/b508541a

[58]Klamt, A.; Schueuermann, G.COSMO: a new approach to dielectric screening in solvents with explicit expressions for the screening energy and its gradient *J. Chem. Soc., Perkin Trans. 2* 1993, 799– 805, DOI: 10.1039/P29930000799

[59]Perdew, J. P.; Burke, K.; Ernzerhof, M.Generalized gradient approximation made simple *Phys. Rev. Lett.* 1996, 77, 3865– 3868, DOI: 10.1103/PhysRevLett.77.3865

[60]Becke, A. D.Density Functional Calculations of Molecular-Bond Energies *J. Chem. Phys.* 1986, 84, 4524– 4529, DOI: 10.1063/1.450025

[61]Perdew, J. P.Density-Functional Approximation for the Correlation-Energy of the Inhomogeneous Electron-Gas *Phys. Rev. B: Condens. Matter Mater. Phys.* 1986, 33, 8822– 8824, DOI: 10.1103/PhysRevB.33.8822

[62]Perdew, J. P.; Tao, J.; Staroverov, V. N.; Scuseria, G. E.Meta-generalized gradient approximation: Explanation of a realistic nonempirical density functional *J. Chem. Phys.* 2004, 120, 6898– 6911, DOI: 10.1063/1.1665298

[63]Staroverov, V. N.; Scuseria, G. E.; Tao, J.; Perdew, J. P.Comparative assessment of a new nonempirical density functional: Molecules and hydrogen-bonded complexes *J. Chem. Phys.* 2003, 119, 12129– 12137, DOI: 10.1063/1.1626543

[64]The "core properties" basis set is derived from the TurboMole DZ basis set developed by Ahlrichs and coworkers. It was obtained from the basis set library under ftp.chemie.uni-karlsruhe.de/pub/basen.

[65]Kutzelnigg, W.; Fleischer, U.; Schindler, M. *The IGLO Method: Ab Initio Calculation and Interpretation of NMR Chemical Shifts and Magnetic Susceptibilities*; Springer-Verlag: Heidelberg, 1990; Vol. 23.

[66]Neese, F.Quantum chemical calculations of spectroscopic properties of metalloproteins and model compounds: EPR and Moessbauer

properties *Curr. Opin. Chem. Biol.* 2003, 7, 125– 135, DOI: 10.1016/S1367-5931(02)00006-6

[67]Neese, F.Prediction of electron paramagnetic resonance g values using coupled perturbed Hartree-Fock and Kohn-Sham theory *J. Chem. Phys.* 2001, 115, 11080– 11096, DOI: 10.1063/1.1419058

[68]Sinnecker, S.; Neese, F.; Noodleman, L.; Lubitz, W.Calculating the electron paramagnetic resonance parameters of exchange coupled transition metal complexes using broken symmetry density functional theory: Application to a Mn(III)/Mn(IV) model compound *J. Am. Chem. Soc.* 2004, 126, 2613– 2622, DOI: 10.1021/ja0390202

[69]Neese, F.Metal and ligand hyperfine couplings in transition metal complexes: the effect of spin-orbit coupling as studied by coupled perturbed Kohn-Sham theory J. Chem. Phys. 2003, 118, 3939– 3948, DOI: 10.1063/1.1540619

[70]Yanai, T.; Tew, D. P.; Handy, N. C.A new hybrid exchange-correlation functional using the Coulomb-attenuating method (CAM-B3LYP) *Chem. Phys. Lett.* 2004, 393, 51– 57, DOI: 10.1016/j.cplett.2004.06.011

[71]Blaesi, E. J.; Fox, B. G.; Brunold, T. C.Spectroscopic and computational Investigation of the H155A variant of cysteine dioxygenase: Geometric and electronic consequences of a third-sphere amino acid substitution *Biochemistry* 2015, 54, 2874– 2884, DOI: 10.1021/acs.biochem.5b00171

[72]Hirata, S.; Head-Gordon, M.Time-dependent density functional theory within the Tamm-Dancoff approximation *Chem. Phys. Lett.* 1999, 314, 291– 299, DOI: 10.1016/S0009-2614(99)01149-5

[73]Hirata, S.; Head-Gordon, M.Time-dependent density functional theory for radicals - An improved description of excited states with substantial double excitation character *Chem. Phys. Lett.* 1999, 302, 375– 382, DOI: 10.1016/S0009-2614(99)00137-2

[74]The geometric parameter τ is defined as $\tau = |(\alpha - \beta)|/60$, where α and β are the two basal angles in pseudo-square-pyramidal geometry. The τ-value is 0.0 in idealized square-planar geometries and 1.0 in idealized but trigonal bipyramidal geometries. For more details, see: Addison, A. W.; Rao, T. N.; Reedijk, J.; Vanrijn, J.; Verschoor, G. C. *J. Chem. Soc., Dalton Trans.* 1984, 1349– 1356, DOI: 10.1039/DT9840001349

[75]Driggers, C. M.; Cooley, R. B.; Sankaran, B.; Hirschberger, L. L.; Stipanuk, M. H.; Karplus, P. A.Cysteine Dioxygenase Structures from pH 4 to 9: Consistent Cys-Persulfenate Formation at Intermediate pH and a Cys-Bound Enzyme at Higher pH *J. Mol. Biol.* 2013, 425, 3121– 3136, DOI: 10.1016/j.jmb.2013.05.028

[76]Zheng, H.; Chruszcz, M.; Lasota, P.; Lebioda, L.; Minor, W.Data mining of metal ion environments present in protein structures *J. Inorg.*

Biochem. 2008, 102, 1765– 1776, DOI: 10.1016/j.jinorgbio.2008.05.006

[77] The C_0/D_0 ratio was calculated using the following expression: $C_0/D_0 = (kT/\beta H)[\Delta\varepsilon_{MCD}/\varepsilon_{abs}]$. The CT bands of complex **2** exhibit C_0/D_0 ratios between 0.05 and 0.10.

[78] Pavel, E. G.; Kitajima, N.; Solomon, E. I. Magnetic circular dichroism spectroscopic studies of mononuclear non-heme ferrous model complexes. Correlation of excited- and ground-state electronic structure with geometry *J. Am. Chem. Soc.* 1998, 120, 3949– 3962, DOI: 10.1021/ja973735l

[79] Gardner, J. D.; Pierce, B. S.; Fox, B. G.; Brunold, T. C. Spectroscopic and Computational Characterization of Substrate-Bound Mouse Cysteine Dioxygenase: Nature of the Ferrous and Ferric Cysteine Adducts and Mechanistic Implications *Biochemistry* 2010, 49, 6033– 6041, DOI: 10.1021/bi100189h

[80] The concentration of O_2 in CH_2Cl_2 at 20 °C is 5.8 mM. Therefore, the second-order rate constants (k_2) for the O_2 reaction are $3.3(7) \times 10^{-2}$ M^{-1} s^{-1} for **1** and $2.1(5) \times 10^{-2}$ M^{-1} s^{-1} for **3**.

[81] Bittner, M. M.; Lindeman, S. V.; Popescu, C. V.; Fiedler, A. T. Dioxygen Reactivity of Biomimetic Fe(II) Complexes with Noninnocent Catecholate, o-Aminophenolate, and o-Phenylenediamine Ligands *Inorg. Chem.* 2014, 53, 4047– 4061, DOI: 10.1021/ic403126p

[82] Mehn, M. P.; Fujisawa, K.; Hegg, E. L.; Que, L. Oxygen activation by nonheme iron(II) complexes: alpha-keto carboxylate versus carboxylate *J. Am. Chem. Soc.* 2003, 125, 7828– 7842, DOI: 10.1021/ja028867f

[83] Kumar, D.; Thiel, W.; de Visser, S. P. Theoretical Study on the Mechanism of the Oxygen Activation Process in Cysteine Dioxygenase Enzymes *J. Am. Chem. Soc.* 2011, 133, 3869– 3882, DOI: 10.1021/ja107514f

[84] For the sake of computational efficiency, DFT studies of the O_2 reactivity were performed using truncated models of **2** and **4** that lack the ethyl ester moiety of **1** and **3**. Calculations the Fe(II) precursors indicate that identity of the $L_{S,N}$ ligand (CysOEt or CysAm) has little impact on coordination geometry and electronic structure.

[85] Schenk, G.; Pau, M. Y. M.; Solomon, E. I. Comparison between the Geometric and Electronic Structures and Reactivities of {FeNO}[7] and {FeO_2}[8] Complexes: A Density Functional Theory Study *J. Am. Chem. Soc.* 2004, 126, 505– 515, DOI: 10.1021/ja036715u

[86] Ye, S.; Riplinger, C.; Hansen, A.; Krebs, C.; Bollinger, J. M.; Neese, F. Electronic Structure Analysis of the Oxygen-Activation Mechanism by FeII- and α-Ketoglutarate (αKG)-Dependent Dioxygenases *Chem. - Eur. J.* 2012, 18, 6555– 6567, DOI: 10.1002/chem.201102829

[87]de Visser, S. P.; Straganz, G. D.Why Do Cysteine Dioxygenase Enzymes Contain a 3-His Ligand Motif Rather than a 2His/1Asp Motif Like Most Nonheme Dioxygenases? *J. Phys. Chem. A* 2009, 113, 1835– 1846, DOI: 10.1021/jp809700f

[88]Pierce, B. S.; Gardner, J. D.; Bailey, L. J.; Brunold, T. C.; Fox, B. G.Characterization of the nitrosyl adduct of substrate-bound mouse cysteine dioxygenase by electron paramagnetic resonance: Electronic structure of the active site and mechanistic implications *Biochemistry* 2007, 46, 8569– 8578, DOI: 10.1021/bi700662d

[89]Berto, T. C.; Speelman, A. L.; Zheng, S.; Lehnert, N.Mono- and dinuclear non-heme iron-nitrosyl complexes: Models for key intermediates in bacterial nitric oxide reductases *Coord. Chem. Rev*. 2013, 257, 244– 259, DOI: 10.1016/j.ccr.2012.05.007

[90]At 77 K the S = 3/2 signal is absent due to rapid relaxation.

[91]Tran, C. T.; Skodje, K. M.; Kim, E.Monomeric dinitrosyl iron complexes: synthesis and reactivity *Prog. Inorg. Chem.* 2014, 59, 339– 379, DOI: 10.1002/9781118869994.ch05

[92]D'Autreaux, B.; Horner, O.; Oddou, J.-L.; Jeandey, C.; Gambarelli, S.; Berthomieu, C.; Latour, J.-M.; Michaud-Soret, I.Spectroscopic Description of the Two Nitrosyl-Iron Complexes Responsible for Fur Inhibition by Nitric Oxide *J. Am. Chem. Soc.* 2004, 126, 6005– 6016, DOI: 10.1021/ja031671a

[93]Tonzetich, Z. J.; Do, L. H.; Lippard, S. J.Dinitrosyl Iron Complexes Relevant to Rieske Cluster Nitrosylation *J. Am. Chem. Soc.* 2009, 131, 7964– 7965, DOI: 10.1021/ja9030159

[94]Speelman, A. L.; Zhang, B.; Silakov, A.; Skodje, K. M.; Alp, E. E.; Zhao, J.; Hu, M. Y.; Kim, E.; Krebs, C.; Lehnert, N.Unusual Synthetic Pathway for an $\{Fe(NO)_2\}^9$ Dinitrosyl Iron Complex (DNIC) and Insight into DNIC Electronic Structure via Nuclear Resonance Vibrational Spectroscopy *Inorg. Chem.* 2016, 55, 5485– 5501, DOI: 10.1021/acs.inorgchem.6b00510

[95]Tsai, M.-L.; Tsou, C.-C.; Liaw, W.-F.Dinitrosyl Iron Complexes (DNICs): From Biomimetic Synthesis and Spectroscopic Characterization toward Unveiling the Biological and Catalytic Roles of DNICs *Acc. Chem. Res*. 2015, 48, 1184– 1193, DOI: 10.1021/ar500459j

[96]Hunt, A. P.; Lehnert, N.Heme-Nitrosyls: Electronic Structure Implications for Function in Biology *Acc. Chem. Res.* 2015, 48, 2117– 2125, DOI: 10.1021/acs.accounts.5b00167

[97]Hayes, R. G.; Ellison, M. K.; Scheidt, W. R.Definitive assignment of the g tensor of [Fe(OEP)(NO)] by single-crystal EPR *Inorg. Chem.* 2000, 39, 3665– 3668, DOI: 10.1021/ic000159c

[98]Praneeth, V. K. K.; Neese, F.; Lehnert, N.Spin Density Distribution in Five- and Six-Coordinate Iron(II)-Porphyrin NO Complexes Evidenced by

Magnetic Circular Dichroism Spectroscopy *Inorg. Chem*. 2005, 44, 2570– 2572, DOI: 10.1021/ic050144k

[99]Praneeth, V. K. K.; Naether, C.; Peters, G.; Lehnert, N.Spectroscopic Properties and Electronic Structure of Five- and Six-Coordinate Iron(II) Porphyrin NO Complexes: Effect of the Axial N-Donor Ligand *Inorg. Chem*. 2006, 45, 2795– 2811, DOI: 10.1021/ic050865j

[100]Lehnert, N.; Scheidt, W. R.; Wolf, M. W.Structure and Bonding in Heme-Nitrosyl Complexes and Implications for Biology *Struct. Bonding (Berlin, Ger.)* 2013, 154, 155– 223, DOI: 10.1007/430_2013_92

[101]Ye, S.; Neese, F.The Unusual Electronic Structure of Dinitrosyl Iron Complexes *J. Am. Chem. Soc.* 2010, 132, 3646– 3647, DOI: 10.1021/ja9091616

[102]Blaesi, E. J.; Gardner, J. D.; Fox, B. G.; Brunold, T. C.Spectroscopic and computational characterization of the NO adduct of substrate-bound Fe(II) cysteine dioxygenase: Insights into the mechanism of O_2 activation *Biochemistry* 2013, 52, 6040– 6051, DOI: 10.1021/bi400825c

Supporting Information

The Supporting Information is available free of charge on the ACS Publications website at DOI: 10.1021/acs.inorgchem.6b01931.

- ^{1}H NMR, electronic absorption, MCD, EPR, UV–vis absorption, and IR spectra, metric parameters for DFT-computed structures, results from TD-DFT calculations, kinetic data, Eyring plot, and VTVH-MCD data (PDF)
- Crystallographic data for **1** and **2** (CIF)

Synthesis, X-ray Structures, Electronic Properties, and O$_2$/NO Reactivities of Thiol Dioxygenase Active-Site Models

Anne A. Fischer,[†] Nuru Stracey,[§] Sergey V. Lindeman,[†] Thomas C. Brunold,[§,*]
and Adam T. Fiedler[†,*]

[†]   *Department of Chemistry, Marquette University, Milwaukee, Wisconsin 53201, United States*

[§]   *Department of Chemistry, University of Wisconsin – Madison, Madison, Wisconsin 53706, United States*

Email contact: adam.fiedler@marquette.edu (A.T.F), brunold@chem.wisc.edu (T.C.B)

Table S1. Summary of X-ray Crystallographic Data Collection and Structure Refinement.

	$1 \cdot CH_3OH$	$2 \cdot CH_3OH \cdot 0.5DCE$
empirical formula	$C_{77}H_{71}BFeN_7O_3PS$	$C_{76}H_{71}BclFeN_7OPS$
formula weight	1272.10	1263.54
crystal system	triclinic	Monoclinic
space group	*P-1*	*P2₁/c*
a, Å	13.7590(4)	19.2143(3)
b, Å	15.7112(4)	21.0046(2)
c, Å	16.5846(5)	17.0445(2)
α, deg	101.548(2)	90
β, deg	105.060(2)	108.0967(14)
γ, deg	102.362(2)	90
V, Å^3	3254.96(14)	6538.68(14)
Z	2	4
ρ_{calc}, g/cm^3	1.298	1.284
λ, Å	1.5418	1.5418
μ, mm^{-1}	2.825	3.152
θ-range, deg	6 to 148	6 to 150
reflections collected	45798	53840
independent reflections	13004 [R_{int} = 0.0256]	13090 [R_{int} = 0.0499]
data/restraints/parameters	13004 / 0 / 840	13090 / 0 / 807
GOF (on F^2)	1.102	1.026
$R1/wR2$ ($I > 2\sigma(I)$) ^{a}	0.0409 / 0.0983	0.0381 / 0.0930
$R1/wR2$ (all data) ^{a}	0.0444 / 0.1005	0.0494 / 0.1003

^{a} $R1 = \Sigma ||F_o| - |F_c|| / \Sigma|F_o|$; $wR2 = [\Sigma w(F_o^2 - F_c^2)^2 / \Sigma w(F_o^2)^2]^{1/2}$

Table S2. Comparison of Metric Parameters obtained by X-ray Crystallography and DFT-Calculations of Complexes **2** and **4**.

	2	**2**	**4** [a]	**4**
Bond Distances (Å)	XRD	DFT	XRD	DFT
Fe1-N1	2.169(2)	2.155	2.153(2)	2.134
Fe1-N3	2.178(2)	2.197	2.110(2)	2.164
Fe1-N5	2.183(2)	2.241	2.249(2)	2.174
Fe1-S1	2.3051(5)	2.290	2.3175(6)	2.299
Fe1-N7	2.248(2)	2.285	2.252(2)	2.301
Bond Angles (deg)				
N1-Fe1-N3	98.67(6)	95.2	95.97(6)	94.3
N1-Fe1-N5	86.32(6)	86.1	86.08(6)	86.3
N1-Fe1-S1	120.73(4)	124.8	129.17(5)	124.0
N1-Fe1-N7	88.43(6)	91.7	90.71(6)	91.7
N3-Fe1-N5	82.88(6)	84.4	82.16(6)	83.7
N3-Fe1-S1	139.15(4)	139.6	134.18(5)	140.8
N3-Fe1-N7	86.20(6)	88.9	87.38(7)	87.9
N5-Fe1-S1	108.23(4)	102.3	105.47(5)	104.7
N5-Fe1-N7	167.03(6)	172.8	168.67(6)	171.3
S1-Fe1-N7	84.64(4)	84.5	84.96(5)	83.5

[a] Data obtained from Sallmann, M.; Braun, B.; Limberg, C., *Chem. Commun.* **2015,** *51*, 6785-6787.

Table S3. Selected Bond Distances (Å) for [FeO$_2$] Species Obtained by DFT Calculations.

	$^{S=3}[\mathbf{2}\text{-}\mathrm{O_2}]^{\mathrm{HS}}$	$^{S=2}[\mathbf{2}\text{-}\mathrm{O_2}]^{\mathrm{HS}}$	$^{S=1}[\mathbf{2}\text{-}\mathrm{O_2}]^{\mathrm{HS}}$	$^{S=1}[\mathbf{2}\text{-}\mathrm{O_2}]^{\mathrm{LS}}$	$^{S=3}[\mathbf{4}\text{-}\mathrm{O_2}]^{\mathrm{HS}}$	$^{S=2}[\mathbf{4}\text{-}\mathrm{O_2}]^{\mathrm{HS}}$	$^{S=1}[\mathbf{4}\text{-}\mathrm{O_2}]^{\mathrm{HS}}$	$^{S=1}[\mathbf{4}\text{-}\mathrm{O_2}]^{\mathrm{LS}}$
Fe1-N1	2.415	2.370	2.219	2.168	2.311	2.292	2.139	2.098
Fe1-N3	2.183	2.201	2.272	2.050	2.125	2.134	2.201	2.021
Fe1-N5	2.253	2.267	2.205	2.138	2.221	2.244	2.142	2.096
Fe1-S1	2.311	2.296	2.267	2.186	2.339	2.329	2.283	2.210
Fe1-N7	2.212	2.254	2.266	2.013	2.216	2.253	2.287	2.019
Fe1-O1	2.155	1.944	2.073	1.931	2.163	1.970	2.061	1.943
O1-O2	1.273	1.279	1.263	1.304	1.284	1.288	1.275	1.311

Table S4. Selected Bond Distances (Å) and Angles (deg) for Fe/NO Species Obtained by DFT Calculations.

	$^{S=3/2}[\mathbf{2}\text{-}\mathbf{NO}]^{6\mathrm{C}}$		$^{S=1/2}[\mathbf{2}\text{-}\mathbf{NO}]^{6\mathrm{C}}$		$^{S=1/2}[\mathbf{2}\text{-}\mathbf{NO}]^{5\mathrm{C}}$	
	BP86	TPSSh	BP86	TPSSh	BP86	TPSSh
Fe1-N1	2.344	2.336	2.166	2.109	2.057	2.053
Fe1-N3	2.213	2.204	2.069	2.055	1.997	1.998
Fe1-N5	2.536	2.487	2.30^{a}	2.413	–	–
Fe1-S1	2.310	2.334	2.262	2.282	2.212	2.220
Fe1-N7	2.295	2.240	2.022	2.025	2.034	2.011
Fe1-N8	1.734	1.789	1.716	1.712	1.689	1.697
N8-O1	1.181	1.169	1.192	1.180	1.181	1.169
Fe-N8-O1	152.5	154.8	142.5	142.4	151.2	152.2

^{a} The Fe1-N5 bond was constrained to a distance of 2.30 Å in the geometry optimization of $^{S=1/2}[\mathbf{2}\text{-}\mathbf{NO}]^{6\mathrm{C}}$ with the BP86 functional.
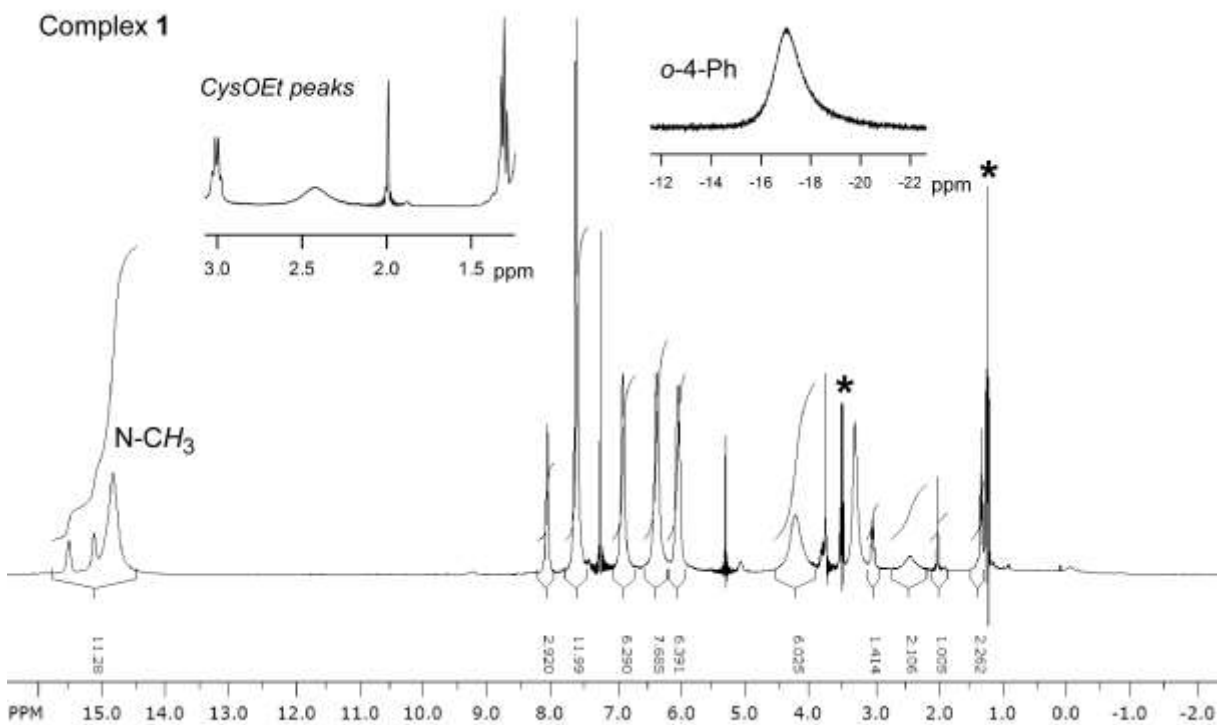
Figure S1. ^{1}H NMR spectrum of complex **1** measured at room temperature in CDCl$_3$. The peaks marked with an asterisk are due to residual NEt$_3$.
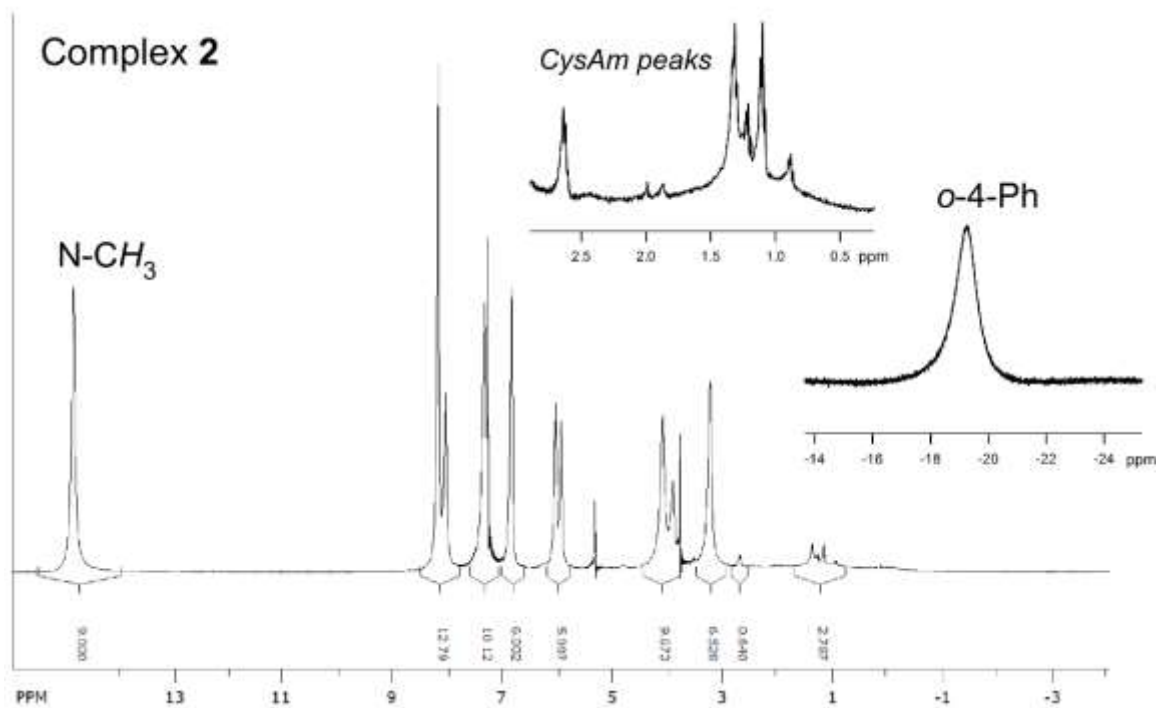

Figure S2. ^{1}H NMR spectrum of complex **2** measured at room temperature in CDCl$_3$.
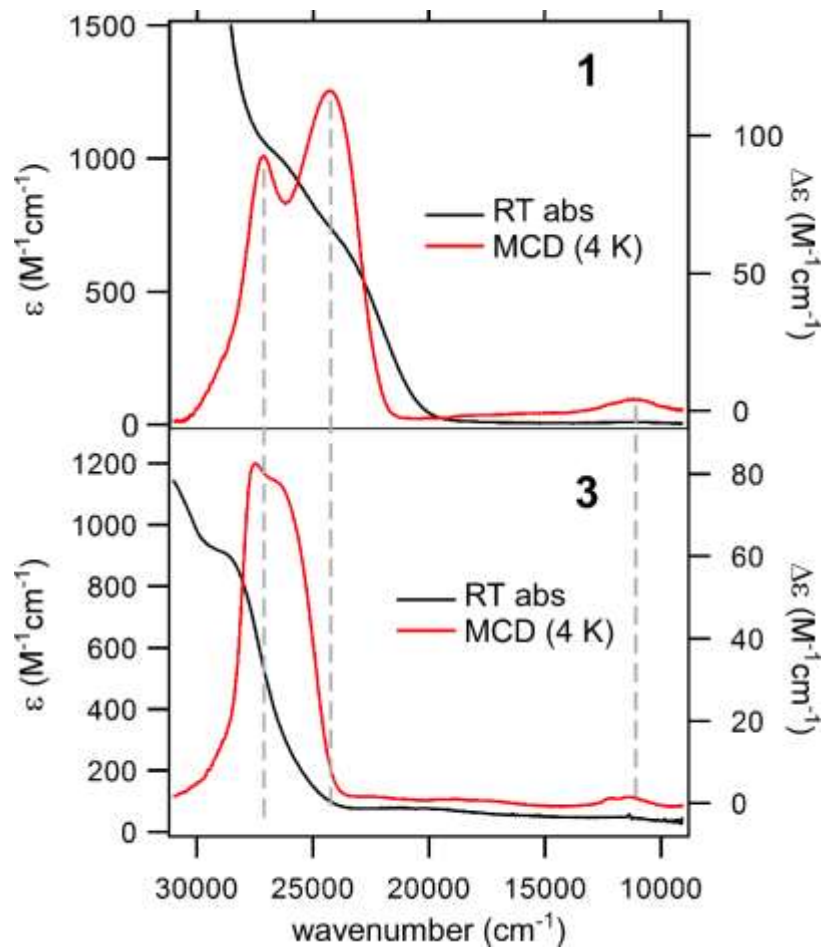
Figure S3. Electronic absorption and MCD spectra collected for complexes **1** (top) and **3** (bottom). The absorption spectra were measured at room temperature in CH_2Cl_2. MCD samples consisted of frozen, glassy solutions in a 3:7 mixture of CH_2Cl_2:butyronitrile; spectra were collected at a temperature of 4 K with a magnetic field of 7 T.
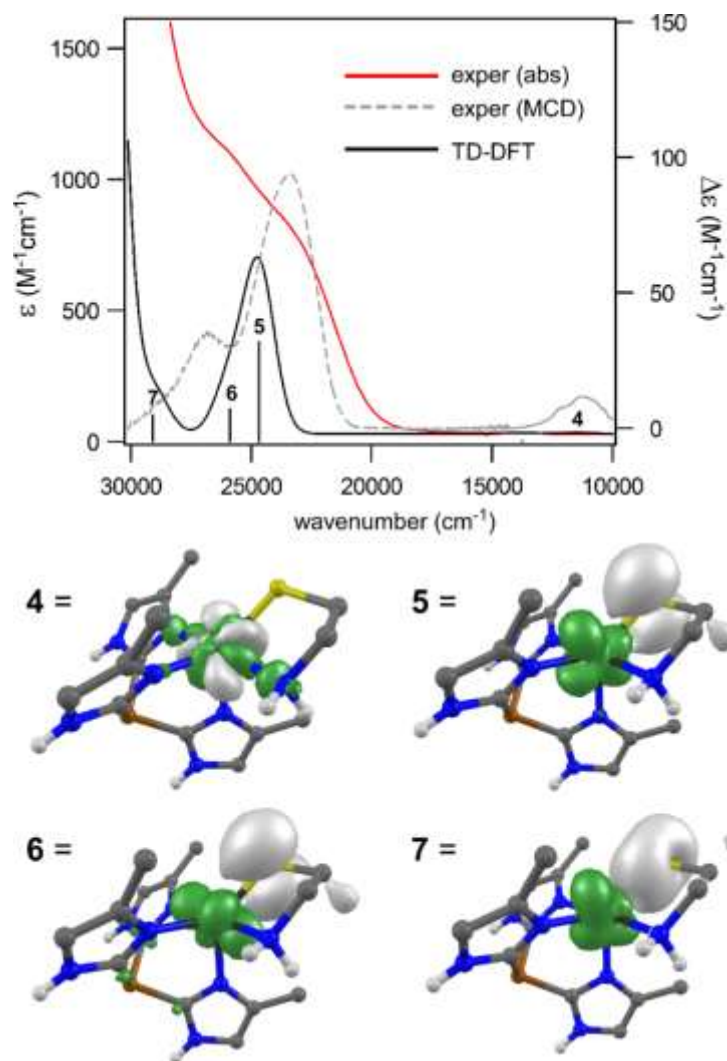
Figure S4. *Top*: TD-DFT computed absorption spectrum of **2** compared to the experimental absorption (red solid line) and MCD (gray dashed line) spectra. The black sticks and numbers mark the energies and intensities of computed transitions. *Bottom*: Electron density difference maps (EDDMs) for computed transitions. The green and grey regions indicate gain and loss of electron density, respectively.
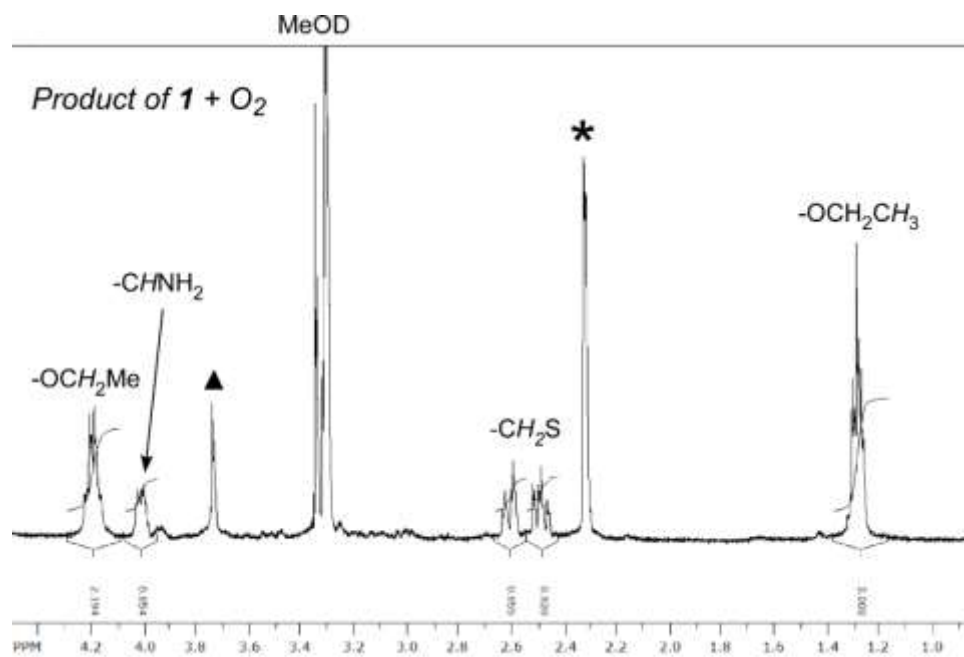
**Figure S5.** ^{1}H NMR spectrum (solvent = CD$_3$OD) of the products isolated from the reaction of **1** with O$_2$ at room temperature. The peak indicated with the asterisk (*) arises from residual toluene, while the peak marked with the triangle (▲) is due to 4,5-diphenyl-1-methyimidazole.
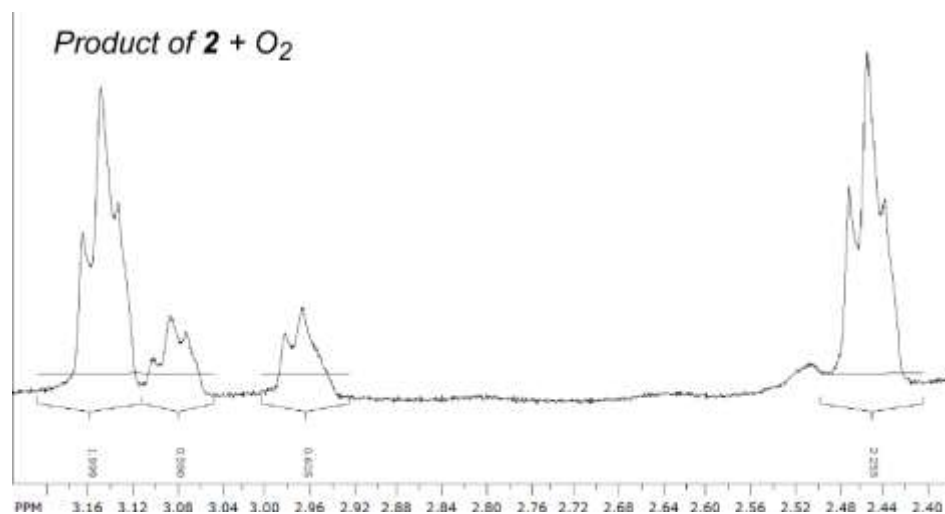
Figure S6. ^{1}H NMR spectrum (solvent = CD$_3$OD) of the products isolated from the reaction of **2** with O$_2$ at room temperature.
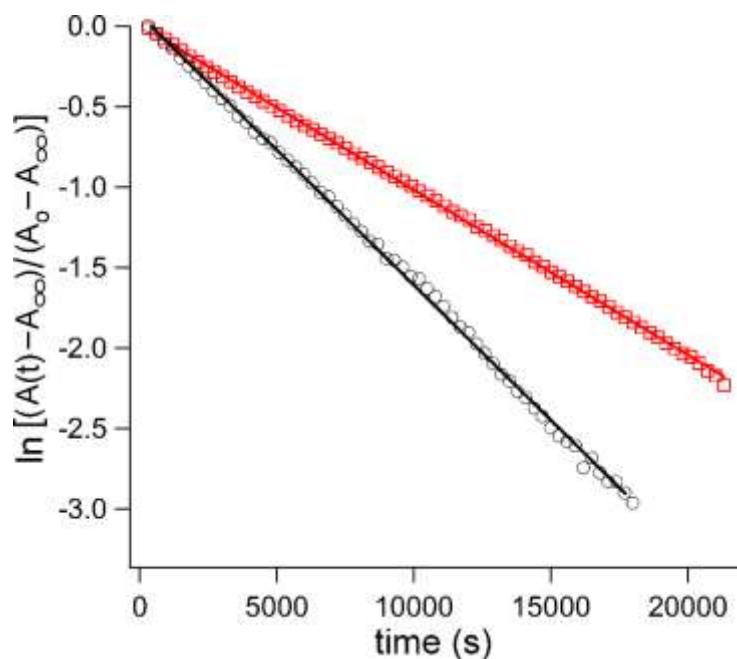
Figure S7. First-order kinetics plots for the reactions of **1** (lower trace, black circle) and **3** (upper trace, red square) with O_2 in O_2-saturated CH_2Cl_2 at 20 $^{\circ}$C. Absorption intensities were monitored at 360 and 355 nm for **1** and **3**, respectively.
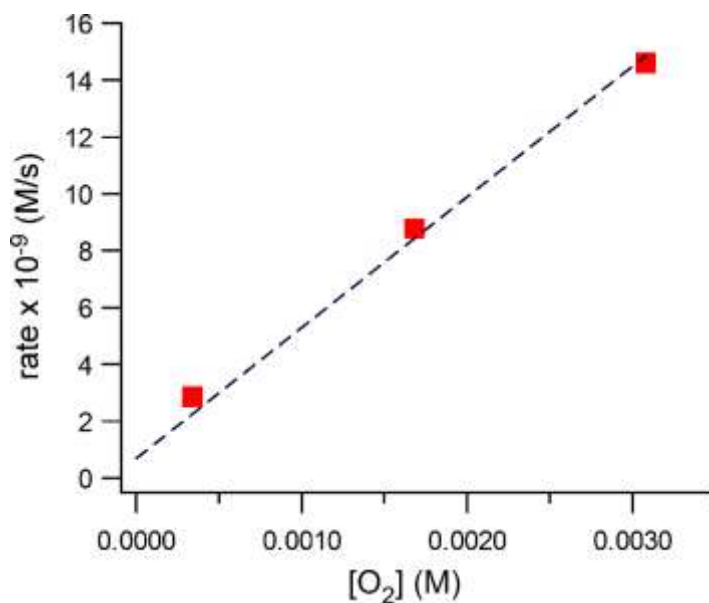

Figure S8. Plots of initial rates versus O_2 concentration for the reaction of complex **1** with O_2 at room temperature in CH_2Cl_2. The Fe concentration was fixed at 0.30 mM.
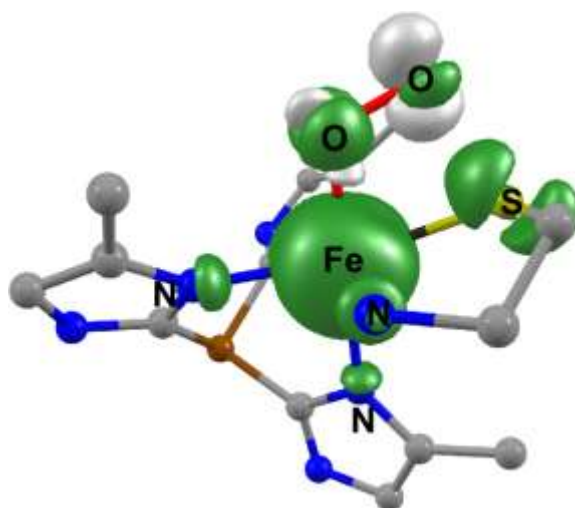
Figure S9. Contour plot of unpaired spin-density in the structure of $^{S=2}$[**2-O$_2$**]^{TS} (*i.e.,* the transition state of the S-O$_d$ bond forming reaction). The green and grey regions indicate regions of excess spin-up (α) and spin-down (β) electron density, respectively.
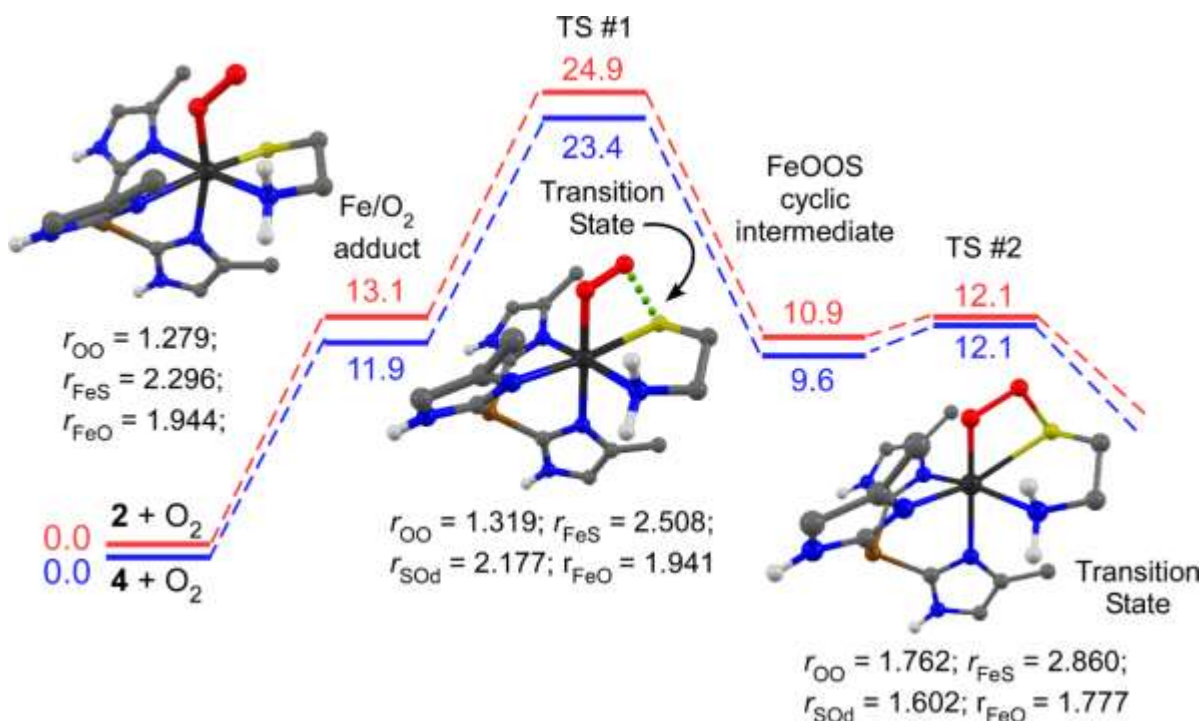

Figure S9. Relative energies (in kcal/mol) for the initial steps in the reaction of **2** (red lines) and **4** (blue lines) with O$_2$ at 298.15 K. Geometry-optimized structures of $^{S=2}$[**2-O$_2$**]^{HS} (left), $^{S=2}$[**2-O$_2$**]^{TS} (middle), and the transition-state for O-O bond cleavage (right) are also provided and select bond lengths are indicated in angstroms (Å).
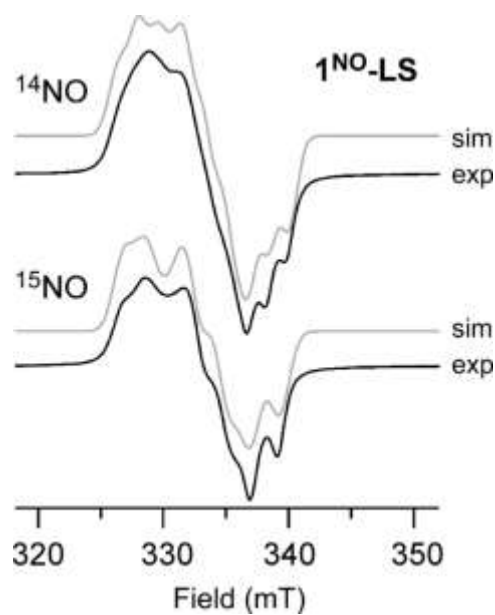
Figure S11. EPR spectra of $\mathbf{1^{NO}}$-**LS** (black solid line) generated via reaction of **1** with [14]NO (top) or [15]NO (bottom) at -70 $^{\circ}$C in CH_2Cl_2. Parameters: frequency = 9.512 GHz; power = 2.0 mW; modulation = 1.0 G; T = 77 K. Simulations of the experimental data (gray lines) were generated using the spin-Hamiltonian parameters listed in Table 3.
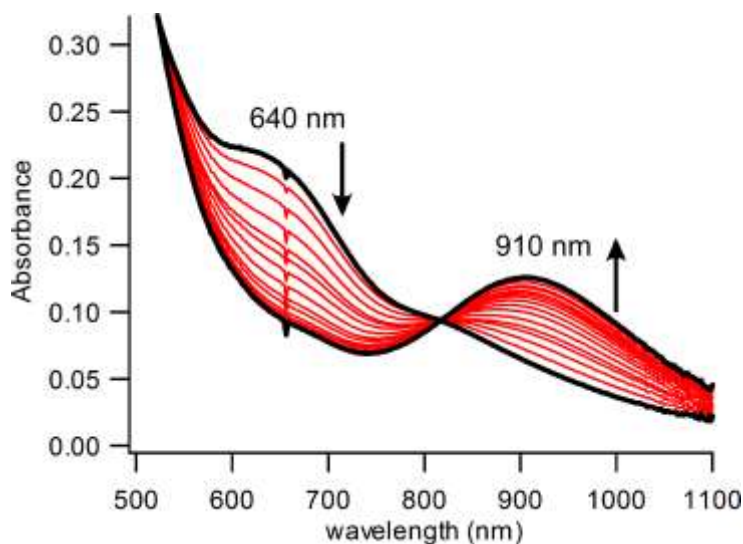

Figure S12. Time-dependent absorption spectra showing the decay of $\mathbf{1^{NO}}$ (λ_{max} = 640 nm) into $\mathbf{RT^{NO}}$ (λ_{max} = 910 nm) at room temperature in CH_2Cl_2.
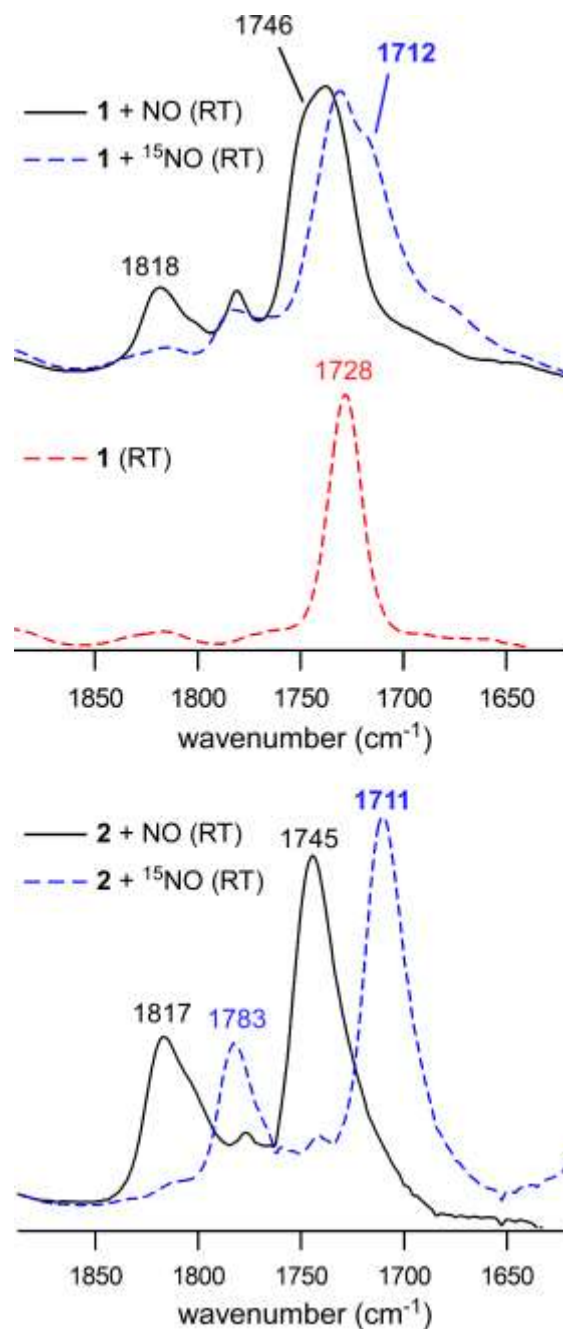
Figure S13. IR spectra measured after treatment of CH_2Cl_2 solutions of **1** or **2** with NO (black solid lines) or ^{15}NO (blue dashed lines) at room temperature. Spectra of NO-treated **1** (top) feature an intense ν(C=O) stretching mode at 1728 cm^{-1} arising from the ester group of the CysOEt ligand.
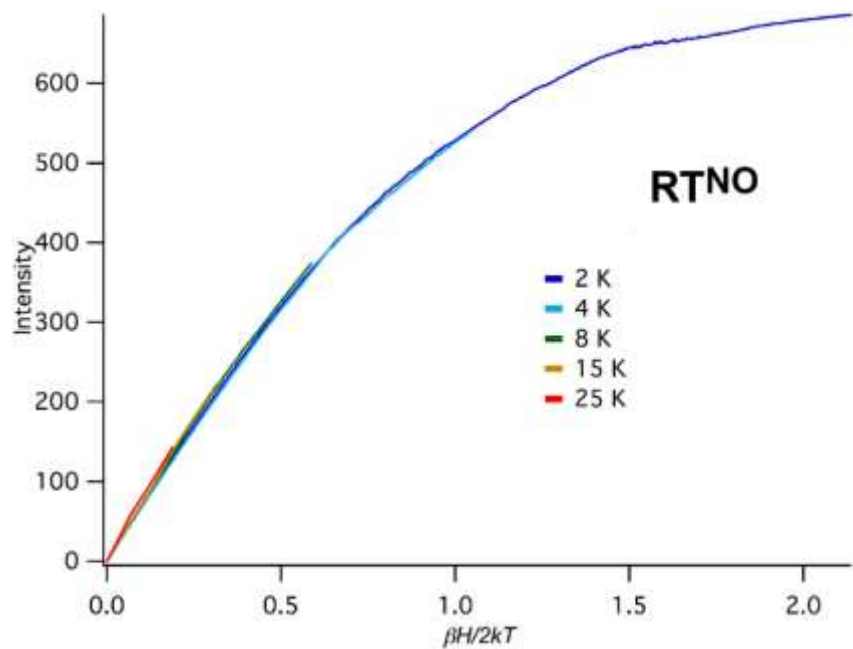
Figure S14. Experimental VTVH-MCD data collected at 907 nm for **RT^{NO}** in a frozen solution of 3:7 CH$_2$Cl$_2$:butyronitrile, plotted against βH/2kT. The experiments were performed by measuring the signal intensity at five temperatures (2, 4, 8, 15, and 25 K) as a function of magnetic field between 0 and 7 T. The observed superposition of the magnetization curves is indicative of a *S* = 1/2 ground state.
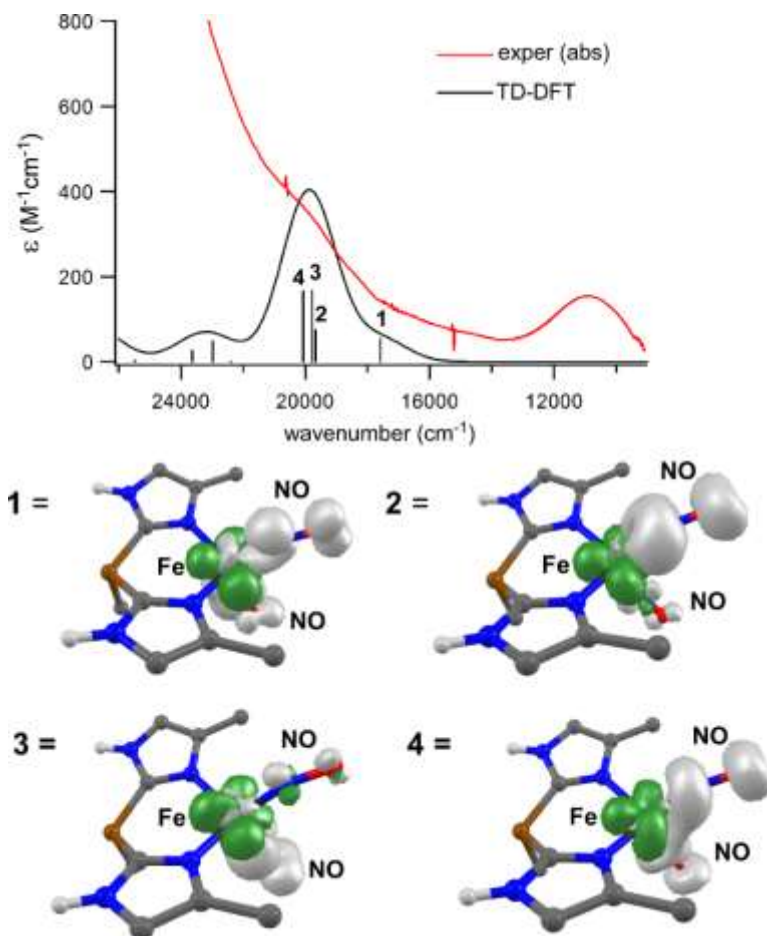
Figure S15. *Top*: TD-DFT computed absorption spectrum of **DNIC^{DFT}** compared to the experimental absorption spectrum of **RT^{NO}** (red solid line). The black sticks and numbers mark the energies and intensities of computed transitions. *Bottom*: Electron density difference maps (EDDMs) for computed transitions. The green and grey regions indicate gain and loss of electron density, respectively.